Impact of multiple modes on the black-hole superradiant instability

Giuseppe Ficarra[*]
Dipartimento di Fisica, "Sapienza" Università di Roma & Sezione INFN Roma1, Piazzale Aldo Moro 5, 00185, Roma, Italy and Department of Physics, King's College London, Strand, London WC2R 2LS, United Kingdom

Paolo Pani[†]
Dipartimento di Fisica, "Sapienza" Università di Roma & Sezione INFN Roma1, Piazzale Aldo Moro 5, 00185, Roma, Italy

Helvi Witek[‡]
Department of Physics, King's College London, Strand, London, WC2R 2LS, United Kingdom

(Received 17 December 2018; published 10 May 2019)

Ultralight bosonic fields in the mass range of approximately $(10^{-20} - 10^{-11})$ eV can trigger a superradiant instability that extracts energy and angular momentum from an astrophysical black hole with mass $M \sim (5, 10^{10})M_\odot$, forming a nonspherical, rotating condensate around it. So far, most studies of the evolution and end state of the instability have been limited to initial data containing only the fastest growing superradiant mode. By studying the evolution of multimode data in a quasiadiabatic approximation, we show that the dynamics is much richer and depends strongly on the energy of the seed, on the relative amplitude between modes, and on the gravitational coupling. If the seed energy is a few percent of the black-hole mass, a black hole surrounded by a mixture of superradiant and nonsuperradiant modes with comparable amplitudes might not undergo a superradiant unstable phase, depending on the value of the boson mass. If the seed energy is smaller, as in the case of an instability triggered by quantum fluctuations, the effect of nonsuperradiant modes is negligible. We discuss the implications of these findings for current constraints on ultralight fields with electromagnetic and gravitational-wave observations.

DOI: 10.1103/PhysRevD.99.104019

I. INTRODUCTION

In classical general relativity, where gravity is minimally coupled to massive bosonic fields, Kerr black holes (BHs) can be unstable against the superradiant instability (for an overview, see Ref. [1]). This process was discovered almost 50 years ago [2–5], but only recently it has been subject to intense scrutiny, including rigorous mathematical proofs [6,7]. It was realized that this instability effectively turns astrophysical BHs into detectors of axionlike particles [8,9] and of ultralight, beyond–standard model bosons in general.

For a BH of mass M and an ultralight boson with mass $m_B \equiv \hbar\mu$, the instability is efficient only when the gravitational coupling $\frac{GM\mu}{c} \sim \mathcal{O}(1)$, i.e., when the Compton wavelength of the particle is comparable to the BH radius. Since astrophysical BHs are expected to exist at least in the mass range $\sim(5, 10^{10})M_\odot$, the superradiant instability is effective for bosons approximately in the mass range $m_B \in (10^{-20} - 10^{-11})$ eV, i.e., for ultralight bosons. The latter are compelling dark-matter candidates[1] and are predicted in a multitude of beyond–standard model scenarios [12–15].

The superradiant instability of a Kerr BH has been investigated perturbatively for scalar fields [16–19], including recent exploration of its phenomenological implications [20–25], more recently for vector and tensor fields in a small-rotation expansion [26–31], and for vector fields around BHs with arbitrary spin in an analytical Newtonian approximation valid for small gravitational coupling [32] and numerically for generic values of the BH spin and gravitational coupling [33,34], also using a novel perturbation scheme [35,36]. Recently, nonlinear simulations[2] of the Einstein equations minimally coupled to complex single-mode vector fields [40–42] have confirmed the analysis of previous quasiadiabatic and perturbative

[*]giuseppe.ficarra@kcl.ac.uk
[†]paolo.pani@roma1.infn.it
[‡]helvi.witek@kcl.ac.uk

[1]The collapse and collision of compact objects composed of these dark-matter candidates has been studied in Refs. [10,11].

[2]The superradiant instability affects also Kerr BHs in asymptotically anti-de Sitter spacetime; see Refs. [37–39] for nonlinear simulations in this context.

evolution [43] (see also Ref. [44]). The latter is justified by the long instability timescale as compared to the dynamical timescale of the BH.

Note that in the case of complex massive bosonic fields or, equivalently, multiple real fields such that the resulting energy-momentum tensor respects the symmetry of the Kerr spacetime, there exist stationary spinning BH solutions surrounded by an oscillating condensate [45,46]. These solutions interpolate between boson stars and Kerr BHs and are formed during the evolution of the superradiant instability of Kerr BHs against complex bosons [40,44]. These solutions are unstable against higher-order azimuthal modes [47] and, at least in some region of their parameter space [48], the instability timescale is comparable to that of Kerr. We deal here with *a single real* bosonic field, so the only stationary BH configuration is the Kerr metric, as guaranteed by the no-hair theorems [49,50].

The general properties of this process do not depend strongly on the nature of the bosonic field; the fundamental unstable mode has a frequency $\omega_R \sim \mu$ (henceforth, we use $G = c = 1$ units) and must satisfy the superradiant condition, $\omega_R < m\Omega_H$, where m is the azimuthal number of the perturbation and Ω_H is the BH angular velocity. As a result of the instability, a single mode with $m > 0$ and arbitrarily small amplitude grows exponentially near the BH, extracting energy and angular momentum on a timescale $\tau \equiv 1/\omega_I \gg M$ and forming a nonspherical, rotating condensate of characteristic size $r_{\rm cloud} \gg M$. Thus, if ultralight bosonic fields exist in nature, they would produce two generic signatures [1,8,9]:

(i) They would favor slowly spinning BHs over highly spinning ones, since BHs would lose their angular momentum over a timescale τ which can be much shorter than the typical BH accretion rate.
(ii) They would produce a continuous gravitational-wave (GW) signal at a frequency set by the boson mass. The first signature translates into the existence of "gaps" in the BH "Regge plane," i.e., in its spin-mass plane [9,26–28,43], whereas the second signature can be directly searched for in LIGO/Virgo (and in the future LISA) data, both as isolated resolvable sources [21,22,32,51–53] and through the GW stochastic background of a population of BH-boson condensates [54].

Most phenomenological studies so far have focused on the idealized case in which the BH is initially surrounded by a *single-mode* superradiant seed (see Ref. [9], in which the generic setup for the evolution of multiple modes has been lain down, although without discussing the phenomenology). However, more realistic configurations are likely to contain a superposition of modes, both superradiant (i.e., satisfying the $\omega_R < m\Omega_H$ condition) and nonsuperradiant. This is particularly important if the initial seed is due to quantum fluctuations, since in that case modes with different values of m are expected to be produced with comparable amplitude.

Full-fledged $3 + 1$ numerical simulations including the backreaction of massive scalar [55] or vector fields [56,57] onto the spacetime employed such *multimode* initial data either through explicit superposition or mode mixing due to the construction of metric initial data. These simulations, furthermore, assumed the presence of an appreciable bosonic cloud, i.e., a condensate of a few percent of the BH mass. Those are formed naturally via the superradiant evolution with small seeds [43]. External effects such as a binary companion or the inspiral and merger of two such BH-condensate systems will cause mode mixing. The merger remnant would form in an environment containing a single cloud with complex multipolar structure; see, e.g., Ref. [23] for work in this direction.

In those cases, the BH was shifted out of the superradiant regime by absorbing a counterrotating mode with sufficiently large amplitude. This essentially switches off the superradiant instability, leaving a rotating BH surrounded by a slowly decaying bosonic condensate. These results indicate that the presence of multiple modes might crucially change the dynamics of the system. However, it is unclear whether this conclusion would persist for arbitrarily small initial seeds. Ideally, one wishes to follow the nonlinear evolution of a small initial seed at least for a few instability e-folding times, $\tau \sim 10^6 M$ ($\tau \sim 10^4 M$), in the most favorable cases for scalars (vectors). These types of simulations are numerically expensive, and, hence, only a small number of cases with timescales of $\sim\mathcal{O}(10^3)M$ were analyzed. Instead, a quasiadiabatic treatment along the lines of Ref. [43] can provide crucial new insight into the evolution of (multimode) massive bosonic clouds surrounding BHs.

That is precisely the goal of this paper: study the impact of multiple modes on the evolution of the superradiant instability. As we shall show, the impact of an initial mixture of nonsuperradiant and superradiant modes with comparable amplitude depends strongly on the energy of the initial seed and on the value of the gravitational coupling $M\mu$. If this energy is initially much smaller than the BH mass (as expected in the most natural scenarios), the effect of multiple modes is negligible. On the other hand, if the energy is at least a few percent of the BH mass and $M\mu \sim \mathcal{O}(0.1)$, the presence of nonsuperradiant modes might affect the evolution and quench the instability completely. As we shall discuss, this latter scenario is more speculative and may comprise only a small fraction of the BH-scalar condensates expected in the Universe.

The rest of this paper is organized as follows. In Sec. II, we introduce our setup and different multimode models and calculate their energy and momentum fluxes. In Sec. III, we present the quasiadiabatic evolution of our systems. We discuss their implications for current electromagnetic and GW-based bounds on the mass of axionlike particles in Sec. IV. We conclude in Sec. V.

II. SETUP

We focus on the action describing a real scalar field Ψ with mass $m_B = \mu\hbar$ minimally coupled to gravity,

$$S = \int d^4x\sqrt{-g}\left(\frac{R}{16\pi} - \frac{1}{2}\partial_\mu\Psi\partial^\mu\Psi - \frac{\mu^2}{2}\Psi^2\right), \quad (1)$$

where g is the determinant of the spacetime metric $g_{\mu\nu}$ and R is the Ricci curvature scalar. Minimization of this action yields the Klein-Gordon equation $\nabla_\mu\nabla^\mu\Psi = \mu^2\Psi$ and Einstein's equations coupled to the stress-energy tensor $T_{\mu\nu} = \partial_\mu\Psi\partial_\nu\Psi - \frac{1}{2}g_{\mu\nu}(\partial_\alpha\Psi\partial^\alpha\Psi + \mu^2\Psi^2)$.

Our setup will be the same as that of Ref. [43]. In particular, we study the quasiadiabatic evolution of the instability, i.e., neglecting the backreaction of the scalar field and instead employing energy balance and angular-momentum balance arguments. Although the total mass of the condensate can reach a few percent of the black-hole mass, the stress-energy tensor (e.g., the energy density) remains small, and our approximation remains valid as shown in Ref. [43]. Furthermore, the energy balance and angular-momentum extraction occurs over the instability timescale, which is much longer than the BH dynamical timescale; this justifies a quasiadiabatic evolution [43,44]. In this regime, the dynamics is governed by the scalar-field equation on a fixed Kerr geometry, the mass and spin of which evolve adiabatically through energy balance and angular-momentum fluxes.

The linearized dynamics of a Klein-Gordon field on the Kerr background with mass M and spin $J = aM = \chi M^2$ is described by the Teukolsky equation for a spin-0 perturbation, the general solution of which can be written as

$$\Psi(t, r, \vartheta, \varphi) = \Re\left[\int d\omega e^{-i\omega t + im\varphi}{}_0S_{lm\omega}(\vartheta)\psi_{lm\omega}(r)\right], \quad (2)$$

where a sum over harmonic indices (l, m) is implicit and ${}_sY_{lm\omega}(\vartheta, \varphi) = {}_sS_{lm\omega}(\vartheta)e^{im\varphi}$ are the spin-weighted spheroidal harmonics of spin weight s, which, for $s = 0$, reduce to the scalar spheroidal harmonics [58]. The radial and angular functions satisfy the following coupled system of differential equations,

$$\begin{aligned}
&\mathcal{D}_\vartheta[{}_0S] + \left[a^2(\omega^2 - \mu^2)\cos^2\vartheta - \frac{m^2}{\sin^2\vartheta} + \lambda\right]{}_0S = 0,\\
&\mathcal{D}_r[\psi] + [\omega^2(r^2 + a^2)^2 - 4aMrm\omega + a^2m^2\\
&\quad - \Delta(\mu^2r^2 + a^2\omega^2 + \lambda)]\psi = 0,
\end{aligned}$$

where for simplicity we omit the (l, m) subscripts, $r_\pm = M \pm \sqrt{M^2 - a^2}$ denotes the coordinate location of the inner and outer horizons, $\Delta = (r - r_+)(r - r_-)$, $\mathcal{D}_r = \Delta\partial_r(\Delta\partial_r)$, and $\mathcal{D}_\vartheta = (\sin\vartheta)^{-1}\partial_\vartheta(\sin\vartheta\partial_\vartheta)$.

A. Unstable modes

Imposing appropriate boundary conditions, namely, purely ingoing waves at the horizon and exponential decay of the scalar field at infinity, a quasibound solution to the above coupled system can be obtained numerically, e.g., using continued fractions [18,59] or a shooting method [60]. The eigenspectrum contains an infinite, discrete set of complex quasibound modes [61], $\omega = \omega_R + i\omega_I$. We will consider only fundamental modes with overtone number $n = 0$, i.e., eigenfunctions with zero nodes. In particular, this system admits unstable ($\omega_I > 0$) quasibound states satisfying the superradiant condition $\omega_R < m\Omega_H$ [18,62], with $\Omega_H = a/(2Mr_+)$ being the angular velocity at the event horizon. For these solutions, the eigenfunctions are exponentially suppressed at spatial infinity,

$$\psi(r) \propto \frac{r^\nu e^{-\sqrt{\mu^2 - \omega^2}r}}{r} \quad \text{as } r \to \infty, \quad (3)$$

where $\nu = M(2\omega^2 - \mu^2)/\sqrt{\mu^2 - \omega^2}$. In the small-coupling limit, $M\mu \ll 1$, these solutions are well approximated by a hydrogenic spectrum [18,62] with angular dependence governed by the spherical harmonics $Y_{lm}(\theta, \phi)$, angular separation constant $\lambda \simeq l(l + 1)$, and frequency

$$\omega \sim \mu - \frac{\mu}{2}\left(\frac{M\mu}{l + 1}\right)^2 + i\frac{\gamma_{lm}}{M}(m\chi - 2\mu r_+)(M\mu)^{4l+5}, \quad (4)$$

where we introduced the dimensionless spin parameter $\chi = a/M = J/M^2$ and the coefficient γ_{lm} is defined by the following relation,

$$\gamma_{lm} = C_l\prod_{j=1}^{l}[j^2(1 - \chi^2) + (m\chi - 2\mu r_+)^2], \quad (5)$$

with $C_l = \frac{2^{4l+1}(2l+1)!}{(l+1)^{2l+4}}\left[\frac{l!}{2l!(2l+1)!}\right]^2$, $C_1 = 1/48$ for the dominant unstable $l = 1$ mode. From Eq. (4), it is clear that these modes become unstable ($\omega_I > 0$) whenever $\omega_R < m\Omega_H$, with an instability timescale roughly given by the e-folding time, $\tau_{lm} = 1/\omega_I$, which strongly depends on the gravitational coupling $M\mu$, dimensionless spin χ, and quantum numbers (l, m).

The critical value of the spin that saturates the superradiance condition reads

$$\chi > \chi_{\text{crit}} \equiv \frac{4mM\mu}{m^2 + 4\mu^2M^2}. \quad (6)$$

In particular, for positive frequencies and spin, $m > 0$ (i.e., a mode corotating with the BH) is a necessary but not sufficient condition for the instability.

In the small-$M\mu$ limit, the radial eigenfunctions read [16,43,63]

$$\psi(r;\mu,\chi,M) \propto g_l(r), \tag{7}$$

where $g_l(r)$ can be written in terms of Laguerre polynomials:

$$g_l(r) = \left(\frac{2rM\mu^2}{l+1}\right)^l \exp\left(-\frac{rM\mu^2}{l+1}\right) L_0^{2l+1}\left(\frac{2rM\mu^2}{l+1}\right). \tag{8}$$

The eigenfunction peaks at

$$r_{\rm cloud} \sim \frac{l(l+1)}{(M\mu)^2} M \tag{9}$$

and thus extends well beyond the horizon, where rotation effects can be neglected.

B. Multiple modes

Using an ansatz of the form (2), we consider a generic superposition of monochromatic modes as

$$\Psi = \sum_{lm} A_{lm} g_l(r) \cos(m\phi - \omega_R t) P_{lm}(\cos\theta), \tag{10}$$

where P_{lm} are the Legendre polynomials. For concreteness, we focus on the lowest-lying modes with the shortest absorption or instability timescales beyond the $l = m = 1$ mode and consider three different cases (cf. Table I),

$$\Psi = \Psi_{11} + A_{1-1} g_1(r) \cos(\phi + \omega_R t) \sin\theta, \tag{11}$$

$$\Psi = \Psi_{11} + A_{22} g_2(r) \cos(2\phi - \omega_R t) \sin^2\theta, \tag{12}$$

$$\Psi = \Psi_{11} + A_{21} g_2(r) \cos(\phi - \omega_R t) \cos\theta \sin\theta, \tag{13}$$

where $\Psi_{11} = A_{11} g_1(r) \cos(\phi - \omega_R t) \sin\theta$. The first case above (dubbed model I) corresponds to the superposition of two modes with $l = 1$ and $m = \pm 1$. The second one (dubbed model II) corresponds to two modes with $l = m = 1, 2$, whereas the third case (dubbed model III) corresponds to the superposition of two modes with the same $m = 1$ but $l = 1, 2$. Note that $\omega_R \sim \mu$ for all modes when $M\mu \ll 1$.

It is convenient to express the initial amplitudes A_{lm} in terms of the total mass of the condensate and the relative amplitude between modes. By introducing the scalar-condensate mass computed in the flat-spacetime approximation (justified in the $M\mu \ll 1$ limit [43,44]),

TABLE I. Initial mode configuration considered in this work.

Model	(l,m) Mode 1	(l,m) Mode 2	Ψ
I	(1, 1)	(1, −1)	Eq. (11)
II	(1, 1)	(2, 2)	Eq. (12)
III	(1, 1)	(2, 1)	Eq. (13)

$$M_S = \int -T_0^0 r^2 \sin\theta {\rm d}r{\rm d}\theta{\rm d}\phi, \tag{14}$$

we obtain

$$A_{11}^2 = \frac{1}{32\pi(1+\lambda_1^2)} \left(\frac{M_S}{M}\right) (M\mu)^4, \tag{15}$$

$$A_{11}^2 = \frac{1}{32\pi(1+81\lambda_2^2)} \left(\frac{M_S}{M}\right) (M\mu)^4, \tag{16}$$

$$A_{11}^2 = \frac{1}{8\pi(4+81\lambda_3^2)} \left(\frac{M_S}{M}\right) (M\mu)^4 \tag{17}$$

for the above three cases, respectively, where we have introduced the relative amplitudes

$$\lambda_1 = \frac{A_{1-1}}{A_{11}}, \qquad \lambda_2 = \frac{A_{22}}{A_{11}}, \qquad \lambda_3 = \frac{A_{21}}{A_{11}}. \tag{18}$$

Thus, each initial state is defined by M_S and by one of the λ_i's, with $\lambda_i \to 0$ being the single $l = m = 1$ mode limit.

C. Energy balance and angular-momentum fluxes

1. GW emission from the scalar condensate

The scalar condensate is a source of GWs. Even though the cloud is nonrelativistic, the quadrupole approximation does not apply because the emission is incoherent [43,63]. Indeed, a dipolar scalar condensate would emit quadrupolar GWs at a frequency $\omega = 2\omega_R \sim 2\mu$, the wavelength of approximately $1/\omega$ of which is generally smaller than the size of the source, $r_{\rm cloud}$. Thus, computing the GW emission requires a fully relativistic computation using the Teukolsky formalism [43,63]. This is performed in the Appendix A; we report the final result here.

For model I ($l = 1$, $m = \pm 1$), we get

$$\dot{E}_{GW} = \frac{1}{160} \frac{1+\lambda_1^4}{(1+\lambda_1^2)^2} \left(\frac{M_S}{M}\right)^2 (M\mu)^{14}, \tag{19}$$

$$\dot{J}_{GW} = \frac{1}{160\omega_R} \frac{1-\lambda_1^2}{1+\lambda_1^2} \left(\frac{M_S}{M}\right)^2 (M\mu)^{14}, \tag{20}$$

for the GW energy balance and angular-momentum fluxes, respectively. Clearly, if $\lambda_1 \to 0$, both expressions reduce to those of the single-mode case with $l = m = 1$ [43]. In the opposite limit, $\lambda_1 \gg 1$, the $m = -1$ mode dominates. This corresponds to the same energy flux, but from Eq. (20), the angular-momentum flux has the opposite sign, as expected for a counterrotating mode. Thus, the angular-momentum variation can be negative when $\lambda_1 > 1$, i.e., when the initial amplitude of the counterrotating mode is bigger than that of the corotating one.

For model II ($l = m = 1, 2$), we get

$$\dot{E}_{GW} = \frac{1}{160(1+81\lambda_2^2)^2}\left(\frac{M_S}{M}\right)^2 (M\mu)^{14}, \tag{21}$$

$$\dot{J}_{GW} = \frac{1}{160\omega_R(1+81\lambda_2^2)^2}\left(\frac{M_S}{M}\right)^2 (M\mu)^{14}. \tag{22}$$

In this case, the angular-momentum variation is always positive because both modes corotate with the BH. When $\lambda_2 \to 0$, we retrieve the $l = m = 1$ single-mode case, while for $\lambda_2 \to \infty$, both expressions are suppressed to leading order in $M\mu \ll 1$.

Finally, for model III ($m = 1$, $l = 1, 2$), we get

$$\dot{E}_{GW} = \frac{1}{10(4+81\lambda_3^2)^2}\left(\frac{M_S}{M}\right)^2 (M\mu)^{14}, \tag{23}$$

$$\dot{J}_{GW} = \frac{1}{10\omega_R(4+81\lambda_3^2)^2}\left(\frac{M_S}{M}\right)^2 (M\mu)^{14}. \tag{24}$$

Again, as $\lambda_3 \to 0$, we obtain the single-mode case, whereas if $\lambda_3 \to \infty$, both expressions are suppressed to leading order in $M\mu \ll 1$. We always neglect the GW energy flux at the horizon, which is typically subdominant [64].

2. Superradiant evolution of the scalar condensate

In the quasiadiabatic approximation, we assume that the energy balance and angular-momentum fluxes of the condensate at the BH horizon $(\dot{E}_S, \dot{J}_S)$ are entirely converted into the growth of the total scalar-cloud mass and angular momentum [43]

$$\dot{E}_S = \dot{M}_S, \tag{25}$$

$$\dot{J}_S = \dot{L}_S, \tag{26}$$

where L_S is the z component of the angular momentum of the cloud. The computation of $\dot{M}_S$ and $\dot{L}_S$ is performed in Appendix B. The procedure can be summarized as follows.

(i) Include an adiabatic time dependence $A_{lm} \to A_{lm}e^{t/\tau_{lm}}$ in the expression for the eigenfunction Ψ; Eq. (10). Note that this yields a time dependence of the relative amplitudes λ_i; cf. Eq. (18) and Eqs. (33)–(35) below.
(ii) Compute $M_S(t)$ and $L_S(t)$ and their corresponding time derivative in the $\omega_I \ll \omega_R$ limit.
(iii) Average the final result over several orbital periods, $T = 2\pi/\omega_R$, of the scalar cloud.

We report the final result here.

For model I ($l = 1$, $m = \pm 1$), we obtain

$$\langle \dot{E}_S \rangle \sim 2M_S \frac{\omega_{11} + \lambda_1^2\omega_{1-1}}{1+\lambda_1^2} \tag{27}$$

$$\langle \dot{J}_S \rangle \sim 2\frac{M_S}{\mu}\frac{\omega_{11} - \lambda_1^2\omega_{1-1}}{1+\lambda_1^2}, \tag{28}$$

where $\langle \ldots \rangle$ is the time average over several orbital periods and we defined $\omega_{lm} \equiv \omega_I$ for a given (l, m). As discussed in detail below, a crucial point is that $\langle \dot{E}_S \rangle < 0$ when λ_1 is sufficiently large, because $\omega_{1-1} < 0$.

For model II ($l = m = 1, 2$), we obtain

$$\langle \dot{E}_S \rangle \sim 2M_S \frac{\omega_{11} + 81\lambda_2^2\omega_{22}}{1+81\lambda_2^2} \tag{29}$$

$$\langle \dot{J}_S \rangle \sim 2\frac{M_S}{\mu}\frac{\omega_{11} + 162\lambda_2^2\omega_{22}}{1+81\lambda_2^2}. \tag{30}$$

Finally, for model III ($m = 1$, $l = 1, 2$), we obtain

$$\langle \dot{E}_S \rangle \sim 2M_S \frac{4\omega_{11} + 81\lambda_3^2\omega_{21}}{4+81\lambda_3^2} \tag{31}$$

$$\langle \dot{J}_S \rangle \sim \frac{1}{\mu}\langle \dot{E}_S \rangle. \tag{32}$$

For a consistency check, we note that all above expressions reduce to the expected limits when $\lambda_i \to 0$ or $\lambda_i \to \infty$.

In the adiabatic approximation, the time dependence of λ_i can be obtained from Eq. (18) and reads

$$\lambda_1(t) = \lambda_1(0)e^{(\omega_{1-1}-\omega_{11})t}, \tag{33}$$

$$\lambda_2(t) = \lambda_2(0)e^{(\omega_{22}-\omega_{11})t}, \tag{34}$$

$$\lambda_3(t) = \lambda_3(0)e^{(\omega_{21}-\omega_{11})t}. \tag{35}$$

III. QUASIADIABATIC EVOLUTION

We are now in the position to study the quasiadiabatic evolution of the BH-scalar condensate in the presence of multiple modes. Using conservation of the total energy and angular momentum, the evolution of the system is described by [43]

$$\begin{cases} \dot{M} + \dot{M}_S = -\dot{E}_{\rm GW} \\ \dot{J} + \dot{L}_S = -\dot{J}_{\rm GW} \\ \dot{M} = -\langle \dot{E}_S \rangle \\ \dot{J} = -\langle \dot{J}_S \rangle \end{cases}. \tag{36}$$

We integrated this simple set of ordinary differential equations (ODEs) using MATHEMATICA with its built-in NDSOLVE function. Using the first relation of Eq. (36), we

TABLE II. Configurations considered in the adiabatic evolution for models I–III.

Case	m_B/eV	$M_0/M_\odot$	μM_0	J_0/M^2	M_{S0}/M_0
A	10^{-18}	10^7	0.075	0.8,0.95	10^{-9}
B	10^{-18}	10^7	0.075	0.8,0.95	0.025
C	4×10^{-18}	10^7	0.299	0.95	0.025

define the residuals of this procedure as Residuals$\equiv \dot{M}+\dot{M}_S+\dot{E}_{\rm GW}$. We varied the working precision of the NDSolve function, which corresponds to changing the resolution of the numerical scheme, and verified that the residuals verified that the residuals remain below 10^{-17}. At variance with Ref. [43], in Eqs. (36), we neglected mass and angular-momentum accretion by ordinary matter (e.g., from an accretion disk), since the latter play a marginal role in the evolution of the system and are not crucial for our purposes. Indeed, accretion simply introduces an extra timescale in the problem, associated with the Salpeter time, $\tau_{\rm accretion}\sim\sigma_T/(4\pi m_p)\sim 4.5\times10^7$ yr, where σ_T and m_p are the Thompson cross section and the proton mass, respectively. The BH mass and spin grow through accretion approximately over this timescale. Thus, a slowly spinning BH that does not satisfy the superradiant condition can be brought into a superradiant phase through accretion [43]. Here, for simplicity, we consider only systems which at $t=0$ satisfy the superradiant condition; including accretion is a straightforward extension that should not affect our overall conclusion. Within our framework, the evolution depends on the dimensionless parameters $M_0\mu\equiv M(t=0)\mu$, $\chi_0\equiv\chi(t=0)$, where $\chi(t)\equiv J(t)/M(t)^2$ is the dimensionless BH spin parameter, and $\lambda_{i,0}\equiv\lambda_i(t=0)$ (with $i=1,2,3$ depending on the model), as well as on the initial scalar-cloud mass $M_{S0}\equiv M_S(t=0)$. The initial angular momentum of the cloud, $L_{S0}\equiv L_S(0)$, is determined in terms of M_{S0}, $\lambda_{i,0}$, and χ_0, as discussed in Appendix B.

For concreteness,[3] we choose to present the numerical results in this section for a BH with mass $M_0=10^7\,M_\odot$ and consider different cases (see also Table II):

(i) Case A: The scalar field has a mass $m_B=10^{-18}$ eV, corresponding to an initial gravitational coupling $M_0\mu\sim0.075$. The initial BH spin is either $\chi_0=0.8$ or $\chi_0=0.95$. In both cases, the BH is initially in a superradiant state, $\Omega_H>\mu/m$. The initial seed has $M_{S0}=10^{-9}M_0$. This is representative for the case $M_{S0}\ll M_0$, which includes seeds due to quantum fluctuations.

(ii) Case B: This is same as case A above but for a seed with larger initial mass $M_{S0}=0.025M_0$, which should model a seed of astrophysical origin, since the energy of the perturbation is a sizeable fraction of the initial BH mass. These configurations are expected, e.g., if an appreciable scalar cloud is already present when the BH forms or if each of the components of a coalescing BH binary are endowed with a scalar cloud.

(iii) Case C: This is same as case B above but for a scalar field with slightly larger mass, $m_B=4\times10^{-18}$ eV, corresponding to an initial gravitational coupling $M_0\mu\sim0.3$. In this case, we set the initial spin to $\chi_0=0.95$ in order to satisfy the superradiant condition initially.

Case A was chosen to agree with the case considered in Ref. [43], whereas case C is representative of the initial data evolved numerically in Ref. [55]. Note that this case is only marginally consistent with our small-coupling approximation, $M\mu\ll1$. In all cases, the BH and boson-field masses correspond to a range that will be accessible by future LISA observations [32,51,52,54].

A. Model I: $l=1$ with $m=\pm1$

1. Case A: Small initial seed

A representative example of the evolution for model I in case A is presented in Fig. 1. In this case, the evolution is insensitive to the presence of a nonsuperradiant unstable mode, even if the latter has initially a much larger amplitude than the superradiant mode [e.g., $\lambda_1(0)=10$]. This is due to Eq. (33); since $\omega_{1-1}<0$ for a nonsuperradiant mode and $\omega_{11}>0$ for the superradiant one, the relative amplitude $\lambda_1(t)$ decreases exponentially over a timescale of approximately $1/(\omega_{1-1}-\omega_{11})$. The evolution is then only affected by the superradiant mode and proceeds as in the $l=m=1$ single-mode case [43]. For the chosen parameters we find $\tau_{11}\sim7\times10^6$ yr which is consistent with the exponential growth of the condensate at $t>10^7$ yr shown in Fig. 1. In this particular case, the condensate extracts about 4% of the initial BH mass. However, its energy density, and hence its backreaction, is negligible [43] so that it dissipates on a longer timescale through GW emission. An estimate for the latter timescale is

$$\tau_{\rm GW}\sim\frac{M_S^{\rm max}}{\dot{E}_{\rm GW}}\sim6\times10^{13}\ {\rm yr}, \tag{37}$$

in agreement with the late-time behavior shown in Fig. 1.

2. Case B: Large initial seed, small coupling

The impact of a nonsuperradiant mode is stronger when the initial seed has a larger amplitude, as illustrated in Fig. 2. There, we show the evolution of model I for fixed $\lambda_{1,0}=1$ and different initial scalar-cloud masses M_{S0}, including case A and case B.

[3]The mass simply sets the scale of the problem, and we could have chosen units such that $M=1$. It is straightforward to consider different values of the BH mass by rescaling all dimensionful quantities accordingly. For example, the evolution for $m_B=10^{-18}$ eV and $M=10^7\,M_\odot$ is equivalent to the evolution for $m_B=10^{-12}$ eV and $M_0=10\,M_\odot$ after rescaling the time coordinate by a factor 10^{-6}.

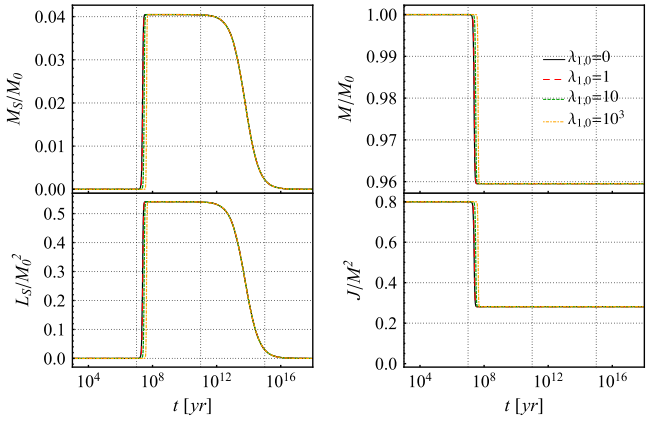

FIG. 1. Evolution of the (a) scalar-cloud mass (top panel) and angular momentum (bottom panel) and (b) BH mass (top panel) and spin (bottom panel) for model I, case A (small initial seeds; cf. Table I) and different initial relative amplitudes $\lambda_{1,0} \equiv \lambda_1(0)$. Note that the evolution is basically insensitive to the presence of a nonsuperradiant mode; i.e., it depends only mildly on the relative initial amplitude $\lambda_{1,0}$.

The case $M_{S0} = 10^{-9} M_0$ corresponds to the case $\lambda_1(0) = 1$ shown in Fig. 1, whereas, as M_{S0} increases, we observe further features. Parts of the scalar cloud are initially absorbed by the BH, the mass of which, in turn, grows in time. This can be understood as follows. Neglecting for the moment GW emission, system (36) reduces to

$$\begin{cases} \dot{M} = -\langle \dot{E}_S \rangle \\ \dot{J} = -\langle \dot{J}_S \rangle \\ \dot{M}_S = \langle \dot{E}_S \rangle \\ \dot{L}_S = \langle \dot{J}_S \rangle \end{cases}, \tag{38}$$

and therefore, when $\langle \dot{E}_S \rangle < 0$ and $\langle \dot{J}_S \rangle < 0$, the mass and angular momentum of the condensate decrease, while the

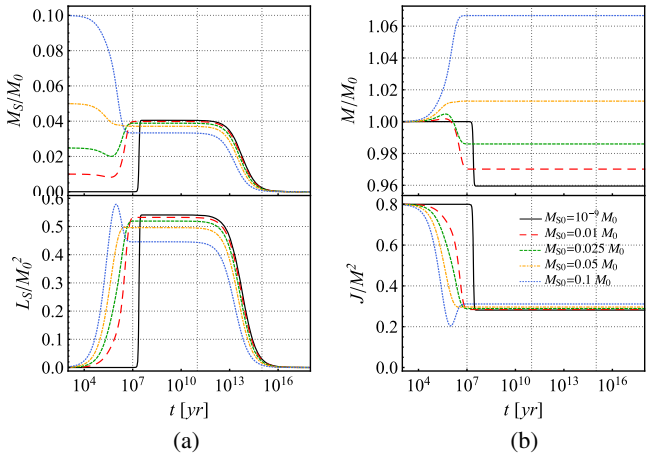

FIG. 2. Same as Fig. 1 for Model I, but for fixed $\lambda_{1,0} = 1$ and different scalar seed amplitudes parametrized by M_{S0}. This includes Case A (black solid line) and Case B (green dashed line).

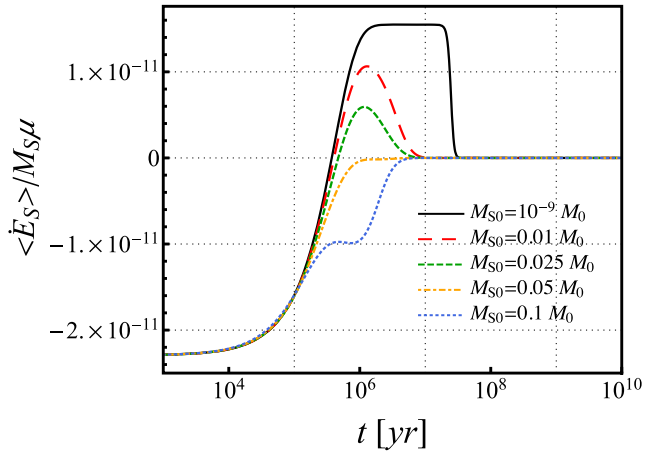

FIG. 3. Evolution of the scalar energy flux (27), rescaled by $M_S\mu$, for $\lambda_{1,0} = 1$ and different inital scalar-cloud masses.

BH mass and spin increase. From Eqs. (27) and (28), this can never happen when $\lambda_1 = 0$, because in that case $\langle \dot{E}_S \rangle, \langle \dot{J}_S \rangle \propto \omega_{11}$ and the scalar fluxes are positive in the superradiant phase (i.e., when $\omega_{11} > 0$). In this case, the instability halts as the superradiant condition is saturated (i.e., as $\Omega_H \to \mu/m$ or, equivalently, as $\omega_{11} \to 0$). However, the situation is different when $\lambda_1 \neq 0$. When $\lambda_1 \ll 1$, Eqs. (27) and (28) reduce to

$$\langle \dot{E}_S \rangle \sim 2M_S[\omega_{11} - (\omega_{11} - \omega_{1-1})\lambda_1^2] + \mathcal{O}(\lambda_1^4), \tag{39}$$

$$\langle \dot{J}_S \rangle \sim 2\frac{M_S}{\mu}[\omega_{11} - (\omega_{11} + \omega_{1-1})\lambda_1^2] + \mathcal{O}(\lambda_1^4), \tag{40}$$

and therefore the energy balance and angular-momentum fluxes are smaller than in the single-mode case as long as $\omega_{11} > |\omega_{1-1}|$.

On the other hand, if $\lambda_{1,0}$ is sufficiently large, it might happen that $\omega_{11} + \lambda_1^2 \omega_{1-1} < 0$, and therefore the scalar energy flux is negative; see Eq. (27). Even when this happens, Eq. (33) shows that $\lambda_1(t)$ decreases exponentially. As shown in Fig. 3 (solid black curve), when the initial seed mass is negligible, the scalar flux can be negative at $t = 0$, but then it turns positive (on a timescale $1/|\omega_{1-1} - \omega_{11}|$) as $\lambda_1(t) \to 0$. Therefore, the usual superradiant evolution is not affected by the presence of a nonsuperradiant mode as long as the initial seed mass is small.

Larger scalar-cloud masses, however, enhance the negative energy flux. This dependence is illustrated in Fig. 3, where we show the energy flux (rescaled by $M_S\mu$) for $\lambda_{1,0} = 1$ and different initial cloud masses. In particular, clouds with intermediate values of M_{S0} such as case B (green dashed line in Figs. 2 and 3) may be partly absorbed, but despite a small increase in the BH mass and decrease of the BH spin, the energy flux becomes positive; i.e., the system reaches the superradiant regime. This picture changes dramatically for larger cloud masses M_{S0}; see,

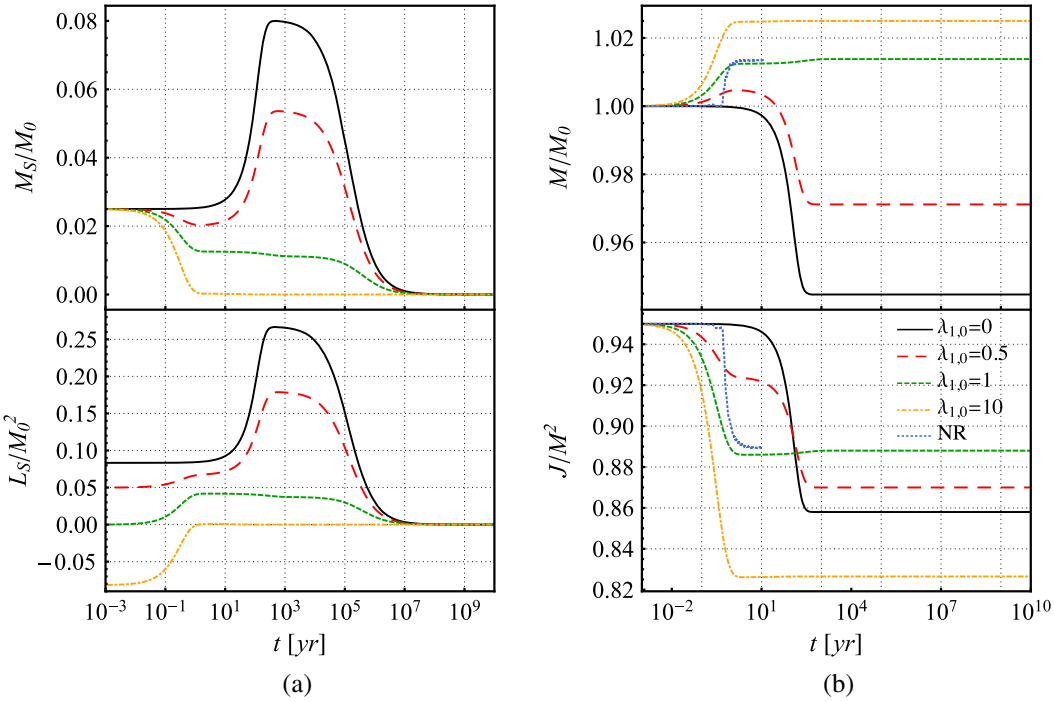

FIG. 4. Same as Fig. 1 but for model I, case C (cf. Table II), i.e., $M_0\mu = 0.3$, $\chi_0 = 0.95$, $M_{S0} = 0.025$, and different $\lambda_{1,0}$. The case $\lambda_{1,0} = 1$ (green dashed line) has the same initial parameters as the fully nonlinear simulation of Ref. [55] indicated by "NR" (blue dotted line). While the BH's early response is different, we recover the same final state. Note that in the case of large relative amplitude, $\lambda_{1,0} = 10$ (yellow dashed lines), the scalar cloud is completely absorbed on short timescales.

e.g., the blue dotted line in Figs. 2 and 3. In such a case, the negative scalar flux is significantly enhanced, a sizeable fraction of the scalar cloud—including its counterrotating modes—is absorbed by the BH, and the superradiant phase can be highly suppressed or entirely absent. The details of the evolution sensitively depend on both the initial relative amplitude $\lambda_{1,0}$ and scalar-cloud mass M_{S0}.

Meanwhile, the angular momentum of the scalar cloud grows because $\langle \dot{L}_S \rangle$ remains positive [see Eq. (28)]. As a result, the BH angular momentum decreases, irrespective of being in the superradiant phase. Interestingly, the final BH spin seems to be similar to the single-mode case. However, a careful investigation of the spin evolution presented in Fig. 5 shows that this is a coincidence. For large enough $\lambda_{1,0}$, the final spin depends crucially on the initial parameters.

3. Case C: Large initial seed, large coupling

When the gravitational coupling $M\mu$ and spin increase, the impact of the seed mass becomes even more relevant. As shown in Fig. 4, the presence of a counterrotating mode with $m = -1$ reduces the superradiant energy extraction. For sufficiently large values of $\lambda_{1,0}$—in the present case $\lambda_{1,0} \geq 1$—the scalar cloud never grows, since the BH absorbs it before superradiance can kick in. At the same time, the BH angular momentum decreases because the absorbed energy is mostly contained in a *counterrotating* mode. Comparing to the critical value $\chi_{\rm crit} \sim 0.882$ [see Eq. (6)], we observe that the system can be driven out of the superradiant regime early in the evolution and therefore does not undergo a superradiant phase.

This behavior agrees with the expectation raised by fully nonlinear simulations [55]. We show their setup *KGl_m30_a3* (cf. Table III of Ref. [55]) as the blue line in Fig. 4. While the immediate response differs due to nonlinear (backreaction) effects, we find excellent agreement within less than 0.5% in the BH mass and spin with the adiabatic evolution at late times.

In these cases, the final BH spin is not only driven by superradiance but also the absorption of counterrotating ($m = -1$) modes. Hence, it depends on the initial parameters as illustrated in Fig. 5. Here, we show the final dimensionless BH spin (relative to its initial value) as a function of $\lambda_{1,0}$ for different initial cloud masses M_{S0}, for cases A and B [Fig. 5(a)] and case C [Fig. 5(b)]. Small perturbations (red solid lines) always yield the superradiant evolution, i.e., BHs of which the final spin is smaller than its initial one due to the superradiant instability independently of the presence of a counterrotating mode. The dependence is more complex for large initial scalar clouds: in an intermediate regime, around $\lambda_{1,0} \lesssim 1$, accretion of counterrotating (i.e., nonsuperradiant) modes and superradiant scattering compete, potentially leading to a larger final spin. Instead, if the initial condensate is dominated by the $m = -1$ mode, the evolution is dominated by accretion

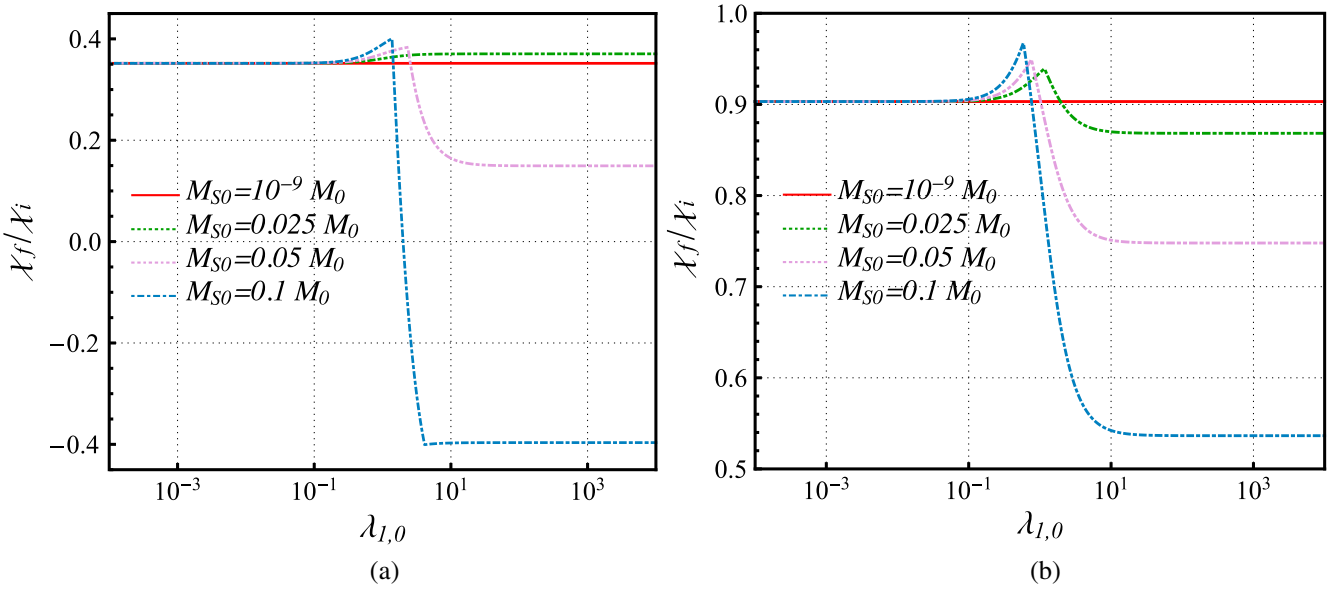

FIG. 5. Ratio between final and initial dimensionless BH spin as a function of the initial relative amplitude $\lambda_{1,0}$ of model I and for different initial scalar-cloud masses M_{S0}. Part (a) corresponds to cases A and B, i.e., has initial parameters ($\chi_0 = 0.8, M_0\mu = 0.075$). Part (b) corresponds to case C, i.e., has ($\chi_0 = 0.95, M_0\mu = 0.3$).

of the counterrotating component and can yield considerably smaller final spins.

To summarize, our quasiadiabatic evolution for model I reveals that the BH superradiant instability proceeds as in the case of a single superradiant mode whenever the seed's energy is negligible (as in the case of quantum fluctuations), whereas the dynamics and the final BH spin are strongly affected by the addition of a nonsuperradiant mode if the latter has a large amplitude relative to the superradiant one and if the initial scalar cloud has a nonnegligible energy. In some extreme cases, the absorption of the counterrotating superradiant mode is sufficient to reduce the BH angular momentum *past* the superradiant condition, so that the instability is completely quenched.

B. Model II: $l = m = 2$ and $l = m = 1$

The phenomenology of model II is different from that of model I. In particular, both modes can trigger the superradiant instability, albeit on vastly different timescales since $\tau \sim (M\mu)^{4l+5}$ depends strongly on l.

We first focus on case A, i.e., small initial fluctuations, the evolution of which is presented in Fig. 6 for different relative amplitudes $\lambda_{2,0}$. We observe two unstable phases: the first one occurring on a timescale $1/\omega_{11}$ and the other occurring on longer scales $1/\omega_{22}$. Because of this separation in timescales, the evolution starts with the first superradiant phase in which the scalar cloud grows and the BH spins down. Then, the cloud is dissipated through GW emission. Finally, the $l = m = 2$ mode becomes unstable, and the scalar cloud grows again, with the BH spin further decreasing since the superradiant threshold $\mu \approx m\Omega$ implies a *smaller* final spin; cf. Eq. (6).

Looking at Fig. 6, it is easy to notice that, regardless of the value of $\lambda_{2,0} \neq 0$, the end state of the system remains unchanged; i.e., the values of the final BH spin and mass are an attractor of the dynamics. In order to better understand this effect, we study the time evolution of $\lambda_2(t)$, which is shown in Fig. 7. After a first depletion occurring at $t \sim \tau_{11}$ due to the superradiant instability induced by the $l = m = 1$ mode, λ_2 undergoes an exponential divergence at $t \sim \tau_{22}$. This can be seen from the definition of $\lambda_2(t)$,

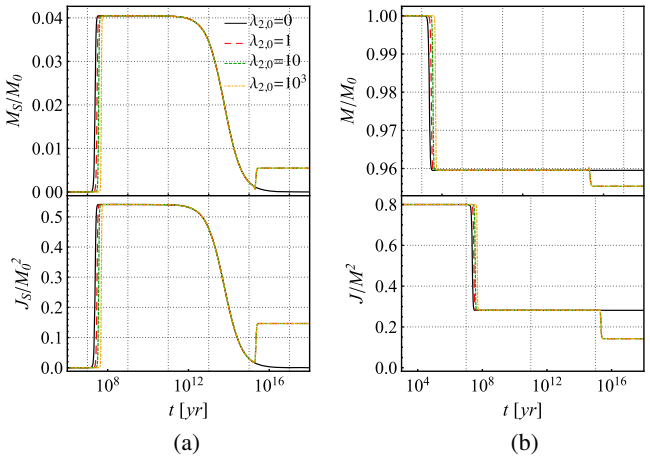

FIG. 6. Same as Fig. 1 but for model II (cf. Table I) and case A (small initial seed), for different values of $\lambda_2(0)$. We observe a first superradiant growth of the scalar cloud (and extraction of BH mass and angular momentum) induced by the dipole mode, followed by dissipation of the cloud due to GW emission. If the quadrupole mode is present, we observe a second superradiant phase independent of the initial relative amplitude $\lambda_{2,0} \neq 0$.

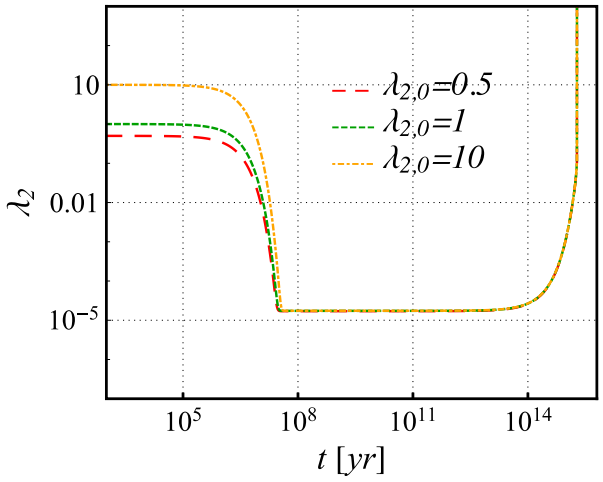

FIG. 7. Evolution of the relative amplitude $\lambda_2(t)$ for model II and different initial values $\lambda_{2,0}$. Note that λ_2 diverges at late times in all cases, corresponding to the second superradiant phase of the $l = m = 2$ mode.

Eq. (34): At $t \sim \tau_{11}$, the system reaches the superradiant threshold of the $l = m = 1$ mode, for which $\omega_{11} = 0$. Afterwards, at $t \sim \tau_{22}$, the secondary mode $l = m = 2$ kicks in and takes the system to the superradiant threshold for the $m = 2$ mode, which is saturated when $\omega_{22} = 0$. In this situation, however, ω_{11} becomes negative, and $\lambda_2(t)$ diverges.

Note that the timescale associated with GW dissipation is much longer for $l = m = 2$ [63], which explains the long time before the condensate disappears (not shown in Fig. 6). For the system under consideration, these long timescales force us to consider an evolution that lasts much longer than the age of the Universe; see Fig. 6. However, if we would consider a stellar-mass BH with $M(0) = 10\ M_\odot$, the timescales would be 10^6 times smaller, since all dimensionful quantities scale with the initial BH mass. Then, also, the secondary superradiant phase might occur within the age of the Universe. Model II, case A is therefore a straightforward interpolation between the case of a single mode with $l = m = 1$ and that of a single mode with $l = m = 2$.

We now focus our attention on the influence of a larger initial scalar cloud. Its evolution is illustrated in Fig. 8 for various M_{S0} and equal initial amplitude of the $l = m = 1$ and $l = m = 2$ modes, i.e., $\lambda_{2,0} = 1$.

As before, we observe the growth of the scalar cloud at the expense of the BH mass and angular momentum on timescales $1/\omega_{11}$, i.e., due to the $l = m = 1$ instability. In contrast to model I, this process is essentially independent of the cloud's initial mass since the influence of the secondary mode kicks in on significantly longer timescales $1/\omega_{22}$. Once the $m = 1$ superradiant threshold is reached, the scalar condensate dissipates via GW emission. Toward the end of this process, after about $t \sim 10^{12}$ yr in our setup, the BH mass *increases*; see Fig. 8(b). This indicates that the scalar cloud is accreted onto the BH.

To better understand this process, let us inspect the energy flux $\sim\omega_{11} + 81\lambda_2^2\omega_{22}$; see Eq. (29) and Fig. 9. Let us also recall the difference in timescales $\omega_{11} \sim (M\mu)^{-9} \gg \omega_{22} \sim (M\mu)^{-13}$. That is, during the early evolution, $\omega_{11} > 0$ dominates, thus triggering the $m = 1$ superradiant instability where the scalar flux is positive and peaks around $\tau \sim 10^6$ yr, as shown in Fig. 9. The scalar's growth stops as the superradiant threshold is reached where $\omega_{11} = 0$, and the clouds start dissipating. Now, although the secondary mode is still growing at a rate $\sim 1/\omega_{22}$ (recall that $\omega_{22} > 0$ is positive), the primary mode starts decaying with a rate $\omega_{11} < 0$. The latter can dominate and lead to a negative scalar energy flux as shown in the inset of Fig. 9. This is consistent with the observation of increasing BH mass in Fig. 8(b).

In the meantime, the relative amplitude between the two modes, $\lambda_2(t) \sim \exp[(\omega_{22} - \omega_{11})t]$, is growing exponentially; see Eq. (34). So, eventually the second term in Eq. (29), which is positive, will cancel and then dominate over the $m = 1$ contribution. At this point, the scalar energy flux is positive, see the inset of Fig. 9, and the BH scalar-cloud configuration undergoes its second (i.e., $m = 2$) superradiant phase. It sets in after about $\tau \sim 10^{13} - 10^{15}$ yr, with the specific onset depending on the scalar-cloud mass; see Fig. 8(a). As expected, the scalar cloud grows by dipping into the BH mass and angular momentum that further decreases the final BH spin. Eventually, the scalar cloud will dissipate via GW emission on timescales much longer than shown in Fig. 8.

C. Model III: $l = 1, 2$ with $m = 1$

Model III is qualitatively similar to model II. In particular, this model interpolates between the single-mode case with $l = m = 1$ (when $\lambda_3 \approx 0$) and the single-mode case with $l = 2$, $m = 1$ (when $\lambda_3 \to \infty$). Also in this case,

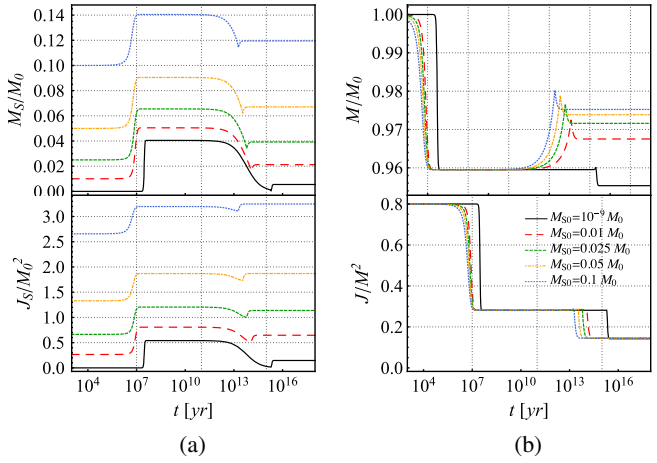

FIG. 8. Same as Fig. 4 but for model II (cf. Table I); i.e., we fixed $\lambda_{2,0} = 1$ and varied the initial scalar-cloud mass M_{S0}. This includes case A (black solid line) and case B (green dashed line).

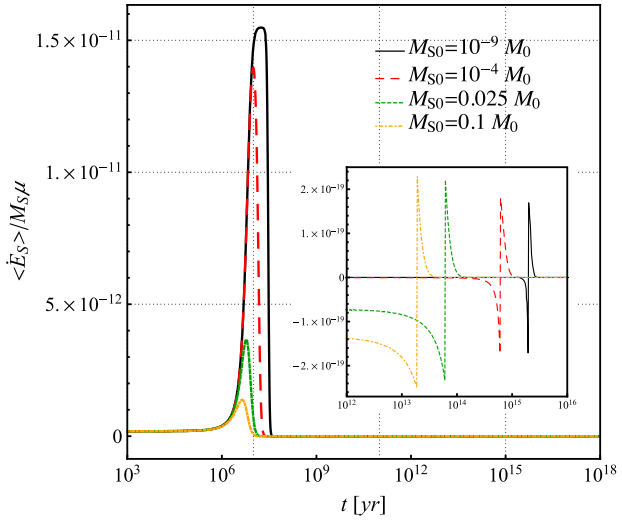

FIG. 9. Evolution of the scalar energy flux, rescaled by the scalar-cloud mass (and mass parameter), for model II. The first peak corresponds to the $m = 1$ superradiant phase. During the following dissipation of the cloud, the $m = 1$ mode decays with $\omega_{11} < 0$ still dominating over the secondary mode. This manifests itself in a *negative* energy flux as shown in the inset. Only when the secondary mode has grown sufficiently, the $m = 2$ superradiant phase kicks in, as indicated by the second (positive) peak in the inset.

the transition occurs for large values of λ_3 because $|\omega_{21}| \ll |\omega_{11}|$. The only qualitative difference is related to the critical value of the spin, which is the same in both regimes, since the modes have the same azimuthal number m and Eq. (6) does not depend on l.

IV. IMPLICATIONS

Due to BH no-hair theorems for real bosonic fields [49,50], the end state of the evolution must be a Kerr BH, the condensate being eventually dissipated in GWs. However, an interesting question concerns the final value of the BH spin in the new stationary configuration and, more generically, the phase space (Regge plane) of the final BH.

Another relevant question concerns the viability of our cases B and C, where the energy of the initial seed is a sizeable fraction (roughly 2%) of the BH mass. This scenario could occur if the BH is formed in a scalar-rich environment, for example if it is formed out of the merger of two previously scalarized BHs. The timescale for GW dissipation of the condensate strongly depends on the coupling [51,52,54]. For the fundamental $l = m = 1$ mode,

$$\tau_{\rm GW} \sim 10^{10} \left(\frac{0.5}{\chi}\right) \left(\frac{M}{10^6\ M_\odot}\right) \left(\frac{0.1}{M\mu}\right)^{15} \text{yr}. \quad (41)$$

Thus, depending on the mass and spin of the BH and on the mass of the bosonic field, $\tau_{\rm GW}$ can easily exceed the age of the Universe, in agreement with Eq. (37) above. In that case, the condensate will not have enough time to dissipate during the coalescence, and the merger remnant will form in an environment where the energy of the scalar field is not negligible.

Although this scenario might be relevant only for a fraction of sources, the majority of supermassive BHs are believed to form via hierarchical mergers. Thus, they constitute a sizeable fraction of the GW signal from bosonic condensates which may potentially be detected by LISA [52,54]. We leave a more quantitative analysis of possible formation scenarios and event rates for future work.

A. Spin evolution

1. Single mode

For reference, let us recall the final spin resulting from the evolution of the single, $l = m = 1$ mode. Focusing on the initial parameters used in our previous sections, the final spin is $\chi(t \to \infty) \approx 0.28$ and $\chi(t \to \infty) \approx 0.86$ for case A and case C, respectively.

2. Model I

The presence of a counterrotating mode can significantly change the value of the final spin, and details depend on the initial parameters. To better understand those dependencies, we present the ratio between the final and initial spin as a function of the initial relative amplitude in Fig. 5. They are shown for different (initial) scalar-cloud masses and fixing ($\chi_0 = 0.8$, $M_0\mu = 0.075$), i.e., model I, cases A and B [see Fig. 5(a)], or ($\chi_0 = 0.95$, $M_0\mu = 0.3$), i.e., model I, case C [see Fig. 5(b)].

If we consider only small fluctuations, this ratio remains constant, i.e., is insensitive to the presence of a counterrotating mode and yields the same final spins as in the single ($l = m = 1$) mode case reviewed above.

Similarly, the final BH spin appears independent of the initial scalar-cloud mass M_{S0} as long as the relative amplitude between counter- and corotating modes is sufficiently small, namely, $\lambda_{1,0} \lesssim 0.1$.

However, if the initial scalar cloud contains comparable excitations of the $m = \pm 1$ modes, i.e., if $\lambda_{1,0} \sim \mathcal{O}(1)$, and its mass is a few percent of the BH's initial mass, the dependency of the final spin is more complex. Now, the angular-momentum flux (28) is determined by both the superradiant $m = +1$ mode and the counterrotating $m = -1$ mode. Since $\omega_{11} > 0$ and $\omega_{1-1} < 0$, both modes will increase the flux and, hence, reduce the final BH spin, although the latter may be slightly larger than in the single $l = m = 1$ mode case, depending on the parameters (see Fig. 5).

As we further increase $\lambda_{1,0} \gtrsim 10$, the ratio between the final and initial BH spin approaches a constant value (i.e., independent of $\lambda_{1,0}$) that can, in fact, be smaller than the

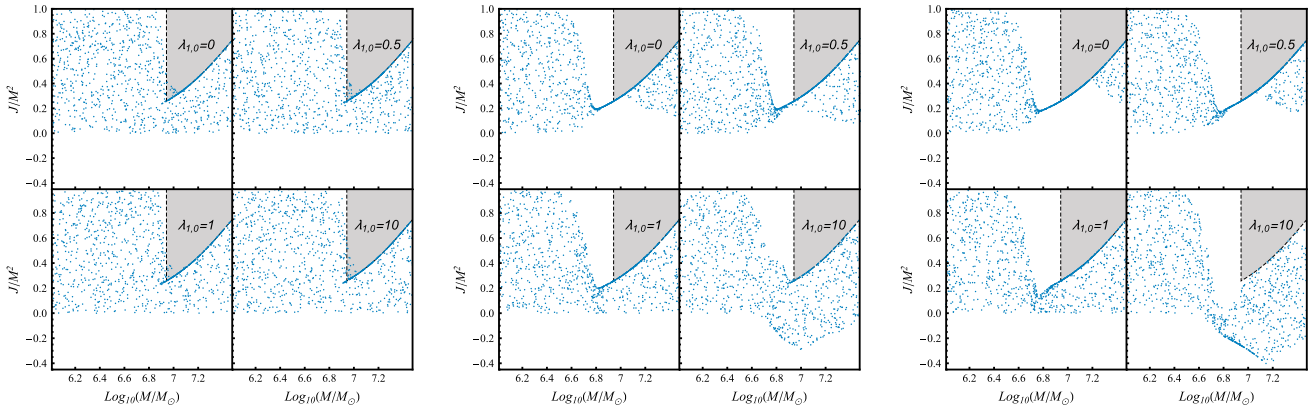

FIG. 10. BH Regge plane [9] obtained from the (adiabatic) evolution of model I, i.e., a scalar field with mass $m_B = 10^{-18}$ eV and containing both co- and counterrotating, $l = 1, m = \pm 1$, modes. We considered scalar-cloud masses of (a) $M_{S0} = 10^{-9} M_0$, (b) $M_{S0} = 0.025 M_0$, and (c) $M_{S0} = 0.05 M_0$ and different initial relative amplitudes $\lambda_{1,0}$. At $t = 0$, we draw the initial BH mass and spin from a random distribution and then follow the evolution up to $t = 10^8$ yr. Each point represents the final BH mass and spin. The shaded area is the Regge gap [9] of the single, $l = m = 1$ superradiant instability, i.e., $\lambda_{1,0} = 0$ as computed in Ref. [43].

$l = m = 1$ case but depends strongly on the initial scalar-cloud mass M_{S0}. Note that the spin can actually flip sign due to absorption of counterrotating modes, as shown in Fig. 5a.

3. Model II

Due to the presence of a secondary superradiant mode, the extraction of the BH spin proceeds in two stages. The first one is caused by the dipole mode and yields the same final BH spin as the single ($l = m = 1$) mode case discussed above. After $t \sim 1/\omega_{22}$, the system undergoes the $l = m = 2$ superradiant phase that yields further extraction of the BH spin. As indicated in Figs. 6 and 8, its final value appears independent of the initial relative amplitude $\lambda_{2,0}$ or scalar-cloud mass M_{S0}. This is because $\lambda_2(t)$ will have acquired the same value (independent of its initial one) by the time the $l = m = 2$ mode becomes active; see Fig. 7. For example, in the case studied here (with $\chi_0 = 0.8$), the final spin is $\chi(t \to \infty) \sim 0.14$.

B. Regge planes

Let us now focus on the mass-spin phase space of the final BH encapsulated in its Regge plot. To identify it, we performed a set of quasiadiabatic evolutions of which the results are shown in Figs. 10–12 for models I and II, respectively. In particular, we considered $m_B = 10^{-18}$ eV and 1000 configurations starting at $t = 0$ with a random distribution of the initial BH spin in the range $\chi_0 \in (0, 0.998)$ and masses in the range $\log_{10} M_0 \in (6, 7.5)$, so that the gravitational coupling $M_0 \mu \in (0.0075, 0.24)$.

For comparison, we show the $\lambda_{i,0} = 0$ case in the top-left panel of each plot in Figs. 10–12. Then, the final BH configuration avoids a specific region of the Regge plane, customarily dubbed the "Regge gap" [9]. For a single (l, m) mode, the shape of this gap is approximately given by [43]

$$\frac{J}{M^2} \gtrsim \chi_{\rm crit} \cup M \gtrsim M_c, \tag{42}$$

where the critical spin $\chi_{\rm crit}$ is given in Eq. (6) and M_c is the value of M that minimizes the spin when $\tau_{lm} = t_F$. An approximate formula is $M_c = (\frac{l+1}{C_l \mu^{4l+6} t_F})^{\frac{1}{4l+5}}$ [43].

1. Model I

We first focus on model I of which the Regge planes are shown in Fig. 10 for initial scalar-cloud masses $M_{S0} = 10^{-9}, 0.025, 0.05 M_0$ and different relative amplitudes $\lambda_{1,0}$. For each initial configuration, we followed the evolution of the system up to $t = t_F = 10^8$ yr $\gg \tau_{11}$.

The evolution of a system containing only small scalar fluctuations $M_{S0} = 10^{-9} M_0$, depicted in Fig. 10(a), is largely independent of the presence of a counterrotating mode. In particular, it exhibits the same exclusion regions in the Regge plane as those induced by the $l = m = 1$ superradiant evolution [43].

If, instead, the scalar cloud already stores a significant fraction of the BH's mass—of the order of a few percent—the spin-mass phase space of the final BH exhibits more structure; see Figs. 10(b) and 10(c). We identify three main features:

(i) We still find gaps in the Regge plane consistent with those of the standard superradiant evolution. However, their onset occurs for smaller masses as the scalar-cloud mass increases, even in the single-mode case. This can be explained by considering that a bigger initial value of the scalar-cloud mass implies a larger energy flux rate via Eq. (27) and,

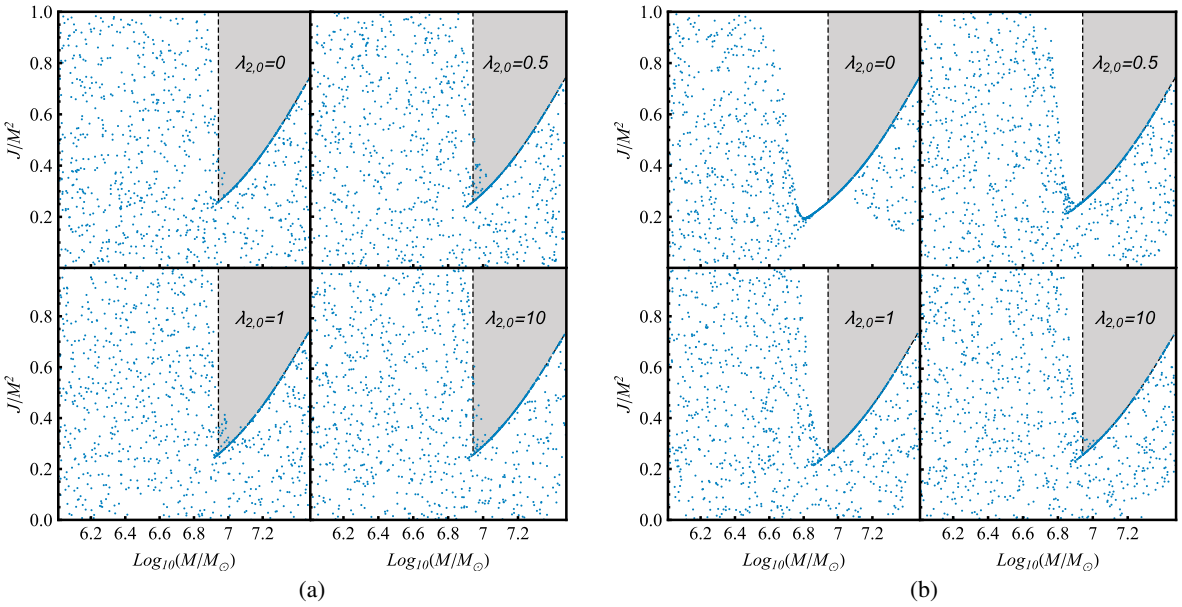

FIG. 11. Same as Fig. 10 but for model II and (a) case A and (b) case B. We evolved the systems for $t_F = 10^8$ yr and different values of the initial relative amplitude $\lambda_{2,0}$. The grey shaded areas denote the Regge gap due to a single, $l = m = 1$ mode.

consequently, a shorter instability timescale. Furthermore, if $\lambda_{1,0} \gtrsim 10$, we start populating the low-mass end of the Regge gap. This is not surprising as the absorption of (counterrotating) modes decreases the BH spin while increasing its mass; see, e.g., Fig. 2.

(ii) We find additional gaps in the Regge plane, just below the superradiant threshold, if the scalar cloud is dominated by the $m = +1$ mode; see the top panels of Figs. 10(b) and 10(c). BHs that are below the threshold will absorb part of the predominantly corotating cloud of which the mass is $\mathcal{O}(1)\%$ of the BH mass. Hence, their mass and spin will increase toward the superradiant threshold. Should they supercede it, the superradiant instability will become active and drive the system toward the threshold from above. That is to say, the superradiant threshold appears to be an attractor if the initial scalar-cloud

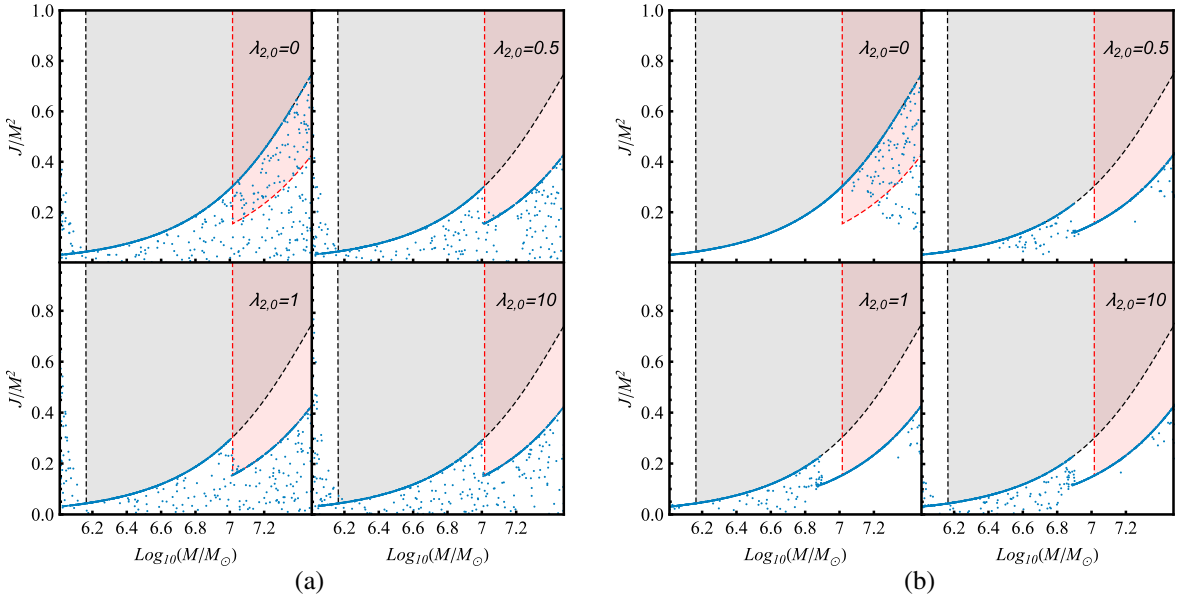

FIG. 12. Same as Fig. 10 but for model II and (a) case A and (b) case B. We evolved the systems for $t_F = 10^{15}$ yr and different initial relative amplitudes $\lambda_{2,0}$. The grey and red shaded areas denote the Regge gap due to a single, $l = m = 1$ and $l = m = 2$ mode, respectively.

mass is sufficiently large and dominated by potentially superradiant (i.e., $m = +1$) modes.

(iii) If the initially large scalar cloud is instead dominated by counterrotating modes, i.e., $\lambda_{1,0} \gtrsim 10$, as shown in the bottom-right panels of Figs. 10(b) and 10(c), these additional holes disappear. Instead, we find BHs with a negative final spin relative to its initial one. This can be understood as follows: BHs that have almost vanishing initial spin will absorb the counterrotating modes that further decrease the BHs' spins. Interestingly, one could now view the system containing a BH with negative spin and cloud with $m = -1$ modes as corotating (but in the opposite direction as before); i.e., the situation is the same as that of a BH with positive spin surrounded by a $m = +1$ cloud. This, again, should suffer from the superradiant instability if the BH is spun up sufficiently. Indeed, the bottom-right panel of Fig. 10(c) seems to exhibit such a new attractor line.

2. Model II

The Regge planes for model II are shown in Figs. 11 and 12 for an evolution time of $t_F = 10^8$ yr $\gg \tau_{11}$ and $t_F = 10^{15}$ yr $\gg \tau_{22}$, respectively. Although the latter timescale is larger than the age of the Universe, it allows us to explore features in the Regge plane due to both the $l = m = 1$ and $l = m = 2$ instability for the supermassive BHs under consideration. Note, furthermore, that this time scales with the BH mass. So, for a much lighter, stellar-mass BH of $\mathcal{O}(10)M_\odot$ (and scalar of $m_B \sim 10^{-12}$ eV), we would observe features of Fig. 12 after $t_F \sim 10^9$ yr.

The Regge plots of Fig. 11 only exhibit the $l = m = 1$ Regge gap since we evolved the systems for times that are significantly shorter than the $l = m = 2$ instability timescale. If the scalar starts off as only a small fluctuation, i.e., case A, the Regge gaps are identical to those of the single, $l = m = 1$ mode. That is, they are independent of the presence of a secondary mode as shown in Fig. 11(a). The Regge gap itself is consistent with the estimate (42).

In Fig. 11(b), we consider a larger cloud with $M_{S0} = 0.025M_0$. As we already saw in model I, the onset of the superradiant instability is shifted toward smaller BH masses as we increase the scalar-cloud mass. In particular, the threshold M_c is a complicated function of the parameters and differs from the expression below Eq. (42). As before, we find an additional gap *below* the superradiant threshold for sufficiently massive scalar clouds; see the top-left panel of Fig. 11(b).

Let us now turn our attention to the long-time evolution depicted in Fig. 12, where we capture both the $l = m = 1$ and $l = m = 2$ phases. For small initial seeds, depicted in Fig. 12(a), we observe the appearance of two Regge gaps consistent, respectively, with the $l = m = 1$ and $l = m = 2$ superradiant evolution. The details are independent of the (initial) relative amplitude $\lambda_{2,0}$ and appear as soon as the secondary mode is switched on.

The Regge plane becomes more complex as we increase the scalar cloud's mass to a few percent of the BH mass; see Fig. 12(b). In particular, we see the formation of a second gap below the superradiant threshold for $l = m = 1$ if $\lambda_{2,0} = 0$ and below the $l = m = 2$ threshold as soon as $\lambda_{2,0} \neq 0$. Again, this can be understood as BHs that start outside the superradiant regime but absorb mass (and angular momentum) from the scalar cloud until they reach the threshold. Finally, the critical mass parametrizing the onset of the superradiant instability decreases, now for the $l = m = 2$ case.

To summarize, even if a scalar condensate surrounding a BH contains counterrotating or higher multipole modes, in all cases studied here, the holes in the Regge plane persist and yield a larger and more complex exclusion region.

V. DISCUSSION

We have investigated the evolution of the BH superradiant instability against ultralight scalar fields with an initial configuration described by a superposition of modes. We focused on the case $M\mu \ll 1$, which allows for a Newtonian description of the condensate and for a quasiadiabatic approximation due to the separation of scales between the instability timescale and the dynamical timescale of the BH.

Our analysis shows that the evolution of the superradiant instability in the presence of an initial superposition of modes is very rich and diverse. The evolution of the system depends strongly on the energy of the scalar seed and on the gravitational coupling $M\mu$. If the seed energy is a few percent of the BH mass, a BH surrounded by a mixture of superradiant and nonsuperradiant modes with comparable amplitudes might not even undergo a superradiant unstable phase, depending on the value of the boson mass.

Our analysis adds to the numerical results of Refs. [55,57], in which the authors explore the interplay between a highly spinning BH and massive scalars or vectors composed of multimode data and with $M\mu \sim \mathcal{O}(0.5)$. Indeed, our simple adiabatic approximation in the small-$M\mu$ limit is in remarkably good agreement with the evolution presented in Ref. [55]. On the other hand, if the seed energy is much smaller than a few percent of the BH mass—as in the most natural and likely scenario in which the instability is triggered by quantum fluctuations—the effect of nonsuperradiant modes is negligible.

This implies that the only case in which the evolution of the superradiant instability is affected by multiple modes is when the BH is initially surrounded by a non-negligible scalar environment, or if it is formed out of the coalescence of two BHs merging with their own scalar clouds. This latter scenario might be relevant only for a fraction of sources, in particular for massive BHs formed out of the merger of two BHs surrounded by their own condensates.

In certain cases, the timescale for GW dissipation of the condensate can exceed the age of the Universe, so a BH might form in a scalar-rich environment. This might be relevant for searches of ultralight fields with LISA [52,54], since supermassive BHs are expected to form hierarchically. In these cases, the initial configuration of ultralight fields around BHs is generically a superposition of (superradiant and nonsuperradiant) modes, and the initial mass of the scalar configuration might be large enough to suppress the instability. We leave a more detailed analysis of such a binary and event rate estimates for future work.

Likewise, the BH Regge plane is also affected by the presence of nonsuperradiant modes when the initial scalar mass is a sizeable fraction of the BH mass. The pattern of the Regge holes is more involved, and additional forbidden regions can appear, depending on the parameters. Interestingly, the region forbidden in the single-mode case is also forbidden in the presence of nonsuperradiant modes; i.e., the original Regge holes are not populated even when the superradiant instability is absent. This is due the absorption of large counterrotating modes which decrease the BH spin.

Our analysis can be extended in several directions. We have neglected mode mixing and possible transfer of energy between modes (e.g., turbulence) which might significantly change the overall picture. We have also neglected scalar self-interactions which—if sufficiently strong—are known to quench the instability and give rise to interesting nonlinear effects such as "bosenovas" [63,65]. Likewise, we have neglected axionlike couplings to the electromagnetic field, which might also quench the instability through a different channel [24,25]. We have also neglected accretion of ordinary matter; in light of the analysis of Ref. [43], we expect that including accretion should be a straightforward extension that would not give a substantial contribution to the understanding of the problem. Furthermore, although we focused on scalar fields, it is likely that the qualitative features of the evolution will be the same also for massive vector (Proca) and massive tensor fields, as indicated by nonlinear simulations that will appear soon [57].

Finally, a natural extension of our work is to investigate whether the presence of multiple modes can also suppress the ergoregion instability of BH mimickers [66–70], since the latter shares [1] many features with the superradiant instability discussed here.

ACKNOWLEDGMENTS

We are indebted to Emanuele Berti, Roberto Emparan, and Vitor Cardoso for important comments on a first draft version of this work and to Richard Brito for relevant comments on the current draft. G. F. wishes to thank King's College London for financial support and the Royal Society for the Ph.D. studentship provided under Research Grant RGF\R1\180073. P. P. acknowledges financial support provided under the European Union's H2020 ERC, Starting Grant, Grant No. DarkGRA–757480, and support from the Amaldi Research Center funded by the MIUR program "Dipartimento di Eccellenza" (CUP: B81I18001170001). H. W. was supported by the European Union's H2020 research and innovation program under Marie Sklodowska-Curie Grant No. BHstabNL-655360 and acknowledges financial support provided by the Royal Society University Research Fellowship UF160547 and Royal Society Research Grant No. RGF\R1\180073. We would like to acknowledge networking support by the COST Action CA16104. H. W. thanks the Yukawa Institute for Theoretical Physics at Kyoto University for its hospitality during the workshop YITP-T-17-02 on "Gravity and Cosmology 2018" and the YKIS2018a symposium on "General Relativity—The Next Generation." We thankfully acknowledge the computer resources at Marenostrum IV, Finis Terrae II, and LaPalma and the technical support provided by the Barcelona Supercomputing Center via the PRACE grant Tier-0 PPFPWG and via the BSC/RES Grants No. AECT-2017-2-0011, No. AECT-2017-3-0009, and No. AECT-2018-1-0014. The authors thankfully acknowledge the computer resources and the technical support provided by the PRACE Grant No. 2018194669 "FunPhysGW: Fundamental Physics in the era of gravitational waves", STFC DiRAC Grant No. ACTP186 "Extreme Gravity and Gravitational Waves" and STFC DiRAC Grant No. ACSP191 "Exploring fundamental fields with strong gravity".

APPENDIX A: GW EMISSION FROM THE SCALAR CONDENSATE

Owing to the separation of scales between the size of the cloud and the BH size for $M\mu \ll 1$, the GW emission can be approximately analyzed by taking the source to lie in a flat[4] background [71]. Because the source is incoherent $1/\omega \ll r_{\rm cloud}$, the quadrupolar approximation fails. In the fully relativistic regime, the gravitational radiation generated is best described by the Teukolsky formalism for gravitational perturbations [72].

1. General two modes case: (l,m) and (l',m')

The gravitational radiation is described by the Newman-Penrose scalar ψ_4, which, in the flat-spacetime approximation, can be decomposed as

[4]We note that the flat-spacetime approximation yields a different prefactor for the GW fluxes emitted from the cloud relative to the case in which the background spacetime is described by a Schwarzschild metric [28,71]. The difference between the two cases is small, and we adopt here a flat-spacetime approximation for simplicity.

$$\psi_4(r,t,\theta,\phi)=\sum_{j=0}^{\infty}\sum_{k=-j}^{j}\int_{-\infty}^{+\infty}\mathrm{d}\omega\frac{R_{jk\omega}(r)}{r^4}{}_{-2}Y_{jk}(\theta,\phi)e^{-i\omega t}, \tag{A1}$$

where the radial function $R_{jk\omega}(r)$ satizsfies the inhomogeneous Teukolsky equation,

$$r^2R''_{jk\omega}-2(r-M)R'_{jk\omega}+[\omega^2r^2-4i\omega(r-3M)-(j+1)(j+2)]R_{jk\omega}=-T_{jk\omega}. \tag{A2}$$

The source term $T_{jk\omega}$ is given by [73]

$$\begin{aligned}\frac{T_{jk\omega}}{2\pi}&=2[(j-1)j(j+1)(j+2)]^{1/2}r^4{}_0T\\&+2[2(j-1)(j+2)]^{1/2}r^2\mathcal{L}(r^3{}_{-1}T)\\&+r\mathcal{L}[r^4\mathcal{L}(r_{-2}T)],\end{aligned} \tag{A3}$$

where we have defined $\mathcal{L}\equiv\partial_r+i\omega$ and

$${}_ST\equiv\frac{1}{2\pi}\int\mathrm{d}\Omega\mathrm{d}t\Theta_S{}_S\bar{Y}_{jk}e^{i\omega t}, \tag{A4}$$

where $\Theta_S=T_{nn},T_{n\bar{m}},T_{\bar{m}\bar{m}}$ for $S=0,-1,-2$, respectively.

The source term $T_{jk\omega}$ is related to the scalar-field stress-energy tensor $T_{\mu\nu}$ through the tetrad projections

$$T_{nn}=T_{\mu\nu}n^\mu n^\nu, \tag{A5}$$

$$T_{n\bar{m}}\equiv T_{\mu\nu}n^\mu\bar{m}^\nu, \tag{A6}$$

$$T_{\bar{m}\bar{m}}\equiv T_{\mu\nu}\bar{m}^\mu\bar{m}^\nu, \tag{A7}$$

where

$$n^\mu\equiv\frac{1}{2}(1,-1,0,0), \tag{A8}$$

$$\bar{m}^\mu\equiv\frac{1}{\sqrt{2}r}\left(0,0,1,-\frac{i}{\sin\vartheta}\right). \tag{A9}$$

For a scalar configuration with two modes with (l,m) and (l',m'), the contributions to the source term are given by a sum over several active modes (j,k), defined by the nonvanishing contributions of the integrals (A4) that are strictly dependent on the values of (l,m) and (l',m'). The contributions will feature two frequencies $\omega=\pm2\omega_R$, due to the fact that $T_{jk\omega}$, computed through Eq. (A3), contains only terms $\propto\delta(\omega\pm2\omega_R)$.

Once the source term is known, the radial equation (A2) can be solved using the Green's function. The latter can be found by considering two linearly independent solutions of the homogeneous equation associated with Eq. (A2), with the following asymptotic behavior [74],

$$R^H\to\begin{cases}r^4e^{-ikr} & r\to0,\\ r^3B_{\rm out}e^{i\omega r}+r^{-1}B_{\rm in}e^{-i\omega r} & r\to\infty,\end{cases} \tag{A10}$$

$$R^\infty\to\begin{cases}A_{\rm out}e^{ikr}+r^4A_{\rm in}e^{-ikr} & r\to0,\\ r^3e^{i\omega r} & r\to\infty,\end{cases} \tag{A11}$$

where $k=\omega-m\Omega_H$, $\{A,B\}_{\rm in,out}$ are constants. Owing to the flat-spacetime approximation, the tortoise coordinate usually defined to deal with these kinds of problems coincides with the standard radial coordinate.

Imposing ingoing boundary conditions at the horizon and outgoing boundary conditions at infinity, one finds that the solution of Eq. (A2) is given by [74]

$$R_{jk\omega}(r)=\frac{R^\infty}{W}\int_0^r\mathrm{d}r'\frac{R^HT_{jk\omega}}{r^4}+\frac{R^H}{W}\int_r^\infty\mathrm{d}r'\frac{R^\infty T_{jk\omega}}{r^4}, \tag{A12}$$

where $W=(R^\infty\partial_rR^H-R^H\partial_rR^\infty)/r=2i\omega B_{\rm in}$ is the Wronskian, which is a constant by virtue of the homogeneous Teukolsky equation. From the asymptotic solution of Eq. (A2), we find

$$B_{\rm in}=-\frac{C_1}{8\omega^2}(j-1)j(j+1)(j+2)e^{i(j+1)\frac{\pi}{2}}, \tag{A13}$$

where C_1 is an arbitrary constant that we set to unity without loss of generality. The solution R^H can be found through

$$R^H=r^2\mathcal{L}(\mathcal{L}r\psi^H), \tag{A14}$$

where ψ^H is the Regge-Wheeler function that at small frequencies reads

$$\psi^H\sim\omega rj_j(\omega r), \tag{A15}$$

where j_j are the spherical Bessel functions of the first kind. At radial infinity, the solutions reads

$$R_{jk\omega}(r\to\infty)\to\frac{R^\infty}{W}\int_0^r\mathrm{d}r'\frac{R^HT_{jk\omega}}{r^4}\equiv\tilde{Z}^\infty_{jk\omega}r^3e^{i\omega r}. \tag{A16}$$

Since the frequency spectrum of the source $T_{jk\omega}$ is discrete with frequencies $\omega=\pm2\omega_R$, $\tilde{Z}^\infty_{jk\omega}$ can be written as

$$\tilde{Z}^\infty_{jk\omega}=\sum_{q=1}^{2}Z^\infty_{jkq}\delta(\omega-\omega_q), \tag{A17}$$

where $\omega_1=2\omega_R$ and $\omega_2=-2\omega_R$. Replacing the above equation in Eq. (A1), we obtain ψ_4 at radial infinity,

$$\psi_4 = \frac{1}{r}\sum_{j=0}^{\infty}\sum_{k=-j}^{j}\sum_{q=1}^{2} Z^{\infty}_{jkq\,-2}Y_{jk}(\theta,\phi)e^{i\omega_q(r-t)}, \tag{A18}$$

which can be written as

$$\psi_4 = \frac{1}{2}(\ddot{h}_+ - i\ddot{h}_\times), \tag{A19}$$

where h_+ and $h_\times$ are the two independent GW polarizations. Then, using Eq. (A18) in the previous relation and integrating twice with respect to the time, we obtain the gravitational waveform:

$$h_+ - ih_\times = \frac{2}{r}\sum_{j=0}^{\infty}\sum_{k=-j}^{j}\sum_{q=1}^{2}\frac{Z^{\infty}_{jkq}}{\omega_q^2}{}_{-2}Y_{jk}(\theta,\phi)e^{i\omega_q(r-t)}. \tag{A20}$$

The energy flux carried by these waves at infinity is given by [4]

$$\frac{d^2E}{dtd\Omega} = \lim_{r\to\infty}\sum_{q=1}^{2}\frac{r^2}{4\pi\omega_q^2}|\psi_4|^2 \equiv \lim_{r\to\infty}\frac{r^2}{16\pi}(\dot{h}_+^2 + \dot{h}_\times^2). \tag{A21}$$

Finally, combining the last two equations, we get the energy balance and angular-momentum fluxes at radial infinity [75],

$$\frac{dE}{dt} \equiv \dot{E}_{GW} = \sum_{j=0}^{\infty}\sum_{k=-j}^{j}\sum_{q=1}^{2}\frac{1}{4\pi\omega_q^2}|Z^{\infty}_{jkq}|^2, \tag{A22}$$

$$\frac{dJ}{dt} \equiv \dot{J}_{GW} = \sum_{j=0}^{\infty}\sum_{k=-j}^{j}\sum_{q=1}^{2}\frac{k}{4\pi\omega_q^3}|Z^{\infty}_{jkq}|^2. \tag{A23}$$

2. Particular cases

We shall now apply the above results to the three models presented in the main text.

a. Model I

For the scalar configuration (11), the contributions to the source term are given by $(j=2, k=\pm 2)$ with two frequencies $\omega = \pm 2\omega_R$, since $T_{jk\omega}$ contains only terms $\propto \delta(\omega \pm 2\omega_R)$. Then, the right-hand sides of Eqs. (A22) and (A23) take the form

$$\sum_{j=0}^{\infty}\sum_{k=-j}^{j}\sum_{q=1}^{2}\frac{|Z^{\infty}_{jkq}|^2}{4\pi\omega_q^2} = \sum_{q=1}^{2}\frac{|Z^{\infty}_{22q}|^2 + |Z^{\infty}_{2-2q}|^2}{4\pi\omega_q^2}, \tag{A24}$$

$$\sum_{j=0}^{\infty}\sum_{k=-j}^{j}\sum_{q=1}^{2}\frac{|Z^{\infty}_{jkq}|^2}{4\pi\omega_q^2} = \sum_{q=1}^{2}\frac{|Z^{\infty}_{22q}|^2 - |Z^{\infty}_{2-2q}|^2}{2\pi\omega_q^3}. \tag{A25}$$

In this particular case, using Eq. (11) and considering the small $M\mu$ limit, we obtain

$$\dot{E}_{GW} = \frac{32\pi^2}{5}(A_{11}^4 + A_{1-1}^4)(M\mu)^6,$$
$$\dot{J}_{GW} = \frac{1}{\omega_R}\frac{32\pi^2}{5}(A_{11}^4 - A_{1-1}^4)(M\mu)^6.$$

Finally, using Eq. (15), we get Eqs. (19) and (20).

b. Model II

For the scalar configuration (12) in Eq. (A3), we have different contributions relative to $(j=2, k=\pm 2)$, $(j=3, k=\pm 3)$, and $(j=4, k=\pm 4)$. Furthermore, the contributions with $k>0$ are $\propto \delta(\omega - 2\omega_R)$, while those with $k<0$ are $\propto \delta(\omega + 2\omega_R)$. In this case, the right-hand sides of Eqs. (A22) and (A23) become

$$\sum_{j=0}^{\infty}\sum_{k=-j}^{j}\sum_{q=1}^{2}\frac{1}{4\pi\omega_q^2}|Z^{\infty}_{jkq}|^2 = \sum_{j=2}^{4}\frac{1}{4\pi\omega_1^2}|Z^{\infty}_{jj1}|^2 + \frac{1}{4\pi\omega_2^2}|Z^{\infty}_{j-j2}|^2, \tag{A26}$$

$$\sum_{j=0}^{\infty}\sum_{k=-j}^{j}\sum_{q=1}^{2}\frac{1}{4\pi\omega_q^2}|Z^{\infty}_{jkq}|^2 = \sum_{j=2}^{4}\frac{j}{4\pi\omega_1^3}|Z^{\infty}_{jj1}|^2 + \frac{(-j)}{4\pi\omega_2^3}|Z^{\infty}_{j-j2}|^2. \tag{A27}$$

Using Eqs. (12), (A26), and (A27) for $M\mu \ll 1$, we get

$$\dot{E}_{GW} = \frac{32}{5}A_{11}^4\pi^2(M\mu)^6 + \frac{16384}{1701}A_{11}^2A_{22}^2\pi^2(M\mu)^8 + \frac{2097152}{413343}A_{22}^4(M\mu)^{10},$$
$$\dot{J}_{GW} = \frac{32}{5\omega_R}A_{11}^4\pi^2(M\mu)^6 + \frac{8192}{567\omega_R}A_{11}^2A_{22}^2\pi^2(M\mu)^8 + \frac{4194304}{413343\omega_R}A_{22}^4(M\mu)^{10}. \tag{A28}$$

Finally, using Eq. (16), the above equations reduce to

$$\dot{E}_{GW} = C_E\left(\frac{M_S}{M}\right)^2(M\mu)^{14}, \tag{A29}$$

$$\dot{J}_{GW} = C_J\left(\frac{M_S}{M}\right)^2(M\mu)^{14}, \tag{A30}$$

with

$$C_E = \frac{413343 + 2560\lambda_2^2(M\mu)^2(243 + 128\lambda_2^2(M\mu)^2)}{66134880(1+81\lambda_2^2)^2},$$
$$C_J = \frac{413343 + 1280\lambda_2^2(M\mu)^2(243 + 512\lambda_2^2(M\mu)^2)}{66134880\omega_R(1+81\lambda_2^2)^2}.$$

The contributions proportional to λ_2 in the numerator are subleading when $M\mu \ll 1$. This implies that, in the considered limit, $\dot{E}_{GW}, \dot{J}_{GW} \propto (M_S/M)^2(M\mu)^{14}$. In this limit, the GW energy balance and angular-momentum fluxes are given by Eqs. (21) and (22).

c. Model III

The stress-energy tensor corresponding to the scalar configuration (12) in Eq. (A3) yields contributions corresponding to $(j=2, k=\pm 2)$, $(j=3, k=\pm 3)$, and $(j=4, k=\pm 4)$. Again, the ones with $k>0$ are $\propto \delta(\omega - 2\omega_R)$, while for $k<0$, they are $\propto \delta(\omega + 2\omega_R)$. The analysis is the same as for model II above; the right-hand sides of Eqs. (A22) and (A23) are given by Eqs. (A26) and (A27).

Finally, considering Eqs. (13), (A26), and (A27) for $M\mu \ll 1$, we get,

$$\begin{aligned}\dot{E}_{GW} &= \frac{32}{5}A_{11}^4\pi^2(M\mu)^6 + \frac{8192}{5103}A_{11}^2A_{21}^2\pi^2(M\mu)^8 \\ &\quad + \frac{524288}{2893401}A_{21}^4(M\mu)^{10}, \\ \dot{J}_{GW} &= \frac{32}{5\omega_R}A_{11}^4\pi^2(M\mu)^6 + \frac{4096}{1701\omega_R}A_{11}^2A_{21}^2\pi^2(M\mu)^8 \\ &\quad + \frac{1048576}{2893401\omega_R}A_{21}^4(M\mu)^{10}. \end{aligned} \tag{A31}$$

Using Eq. (17), the equations above can be written as

$$\dot{E}_{GW} = C_E\left(\frac{M_S}{M}\right)^2(M\mu)^{14}, \tag{A32}$$

$$\dot{J}_{GW} = C_J\left(\frac{M_S}{M}\right)^2(M\mu)^{14}, \tag{A33}$$

with

$$\begin{aligned} C_E &= \frac{2893401 + 1280\lambda_3^2(M\mu)^2(567 + 64\lambda_3^2(M\mu)^2)}{28934010(4+81\lambda_3^2)^2}, \\ C_J &= \frac{2893401 + 640\lambda_3^2(M\mu)^2(1701 + 256\lambda_3^2(M\mu)^2)}{28934010\omega_R(4+81\lambda_3^2)^2}. \end{aligned}$$

Once again, the contributions $\propto \lambda_3$ in the numerator are subleading when $M\mu \ll 1$ and can be neglected, finally obtaining Eqs. (23) and (24).

APPENDIX B: SCALAR ENERGY BALANCE AND ANGULAR-MOMENTUM FLUXES AT THE HORIZON

In this section, we compute the adiabatic time variation of the mass M_S and angular momentum L_S of the condensate due to the superradiant instability.

In the Newtonian approximation, the condensate mass is given by Eq. (14), whereas the z-component of the angular momentum of the condensate reads

$$L_S = \int \mathrm{d}r\mathrm{d}\theta\mathrm{d}\phi r^2 \sin\theta(xT^{0y} - yT^{0x}), \tag{B1}$$

where the quantity $xT^{0y} - yT^{0x}$ has to be expressed in spherical coordinates.

In order to include an adiabatic time dependence, we make the substitution $A_{lm} \to A_{lm}e^{t/\tau_{lm}}$ in the expression (10) of the mode Ψ. Clearly, $\tau_{lm} > 0$ in the superradiant phase, whereas $\tau_{lm} < 0$ otherwise.

1. Model I: $l=1$ and $m=\pm 1$

We start analyzing the case of a scalar cloud described by Eq. (11). Including the time dependence, the expression of the scalar cloud reads

$$\begin{aligned}\Psi &= A_{11}e^{\omega_{11}t}g_1(r)\cos(\phi - \omega_R t)\sin\theta \\ &\quad + A_{1-1}e^{\omega_{1-1}t}g_1(r)\cos(\phi + \omega_R t)\sin\theta, \end{aligned} \tag{B2}$$

where we recall that $\omega_{lm} \equiv \omega_I$ with a given value of (l, m). Using Eq. (14), we obtain

$$M_S(t) = \frac{32\pi M}{(M\mu)^4}(A_{11}^2e^{2\omega_{11}t} + A_{1-1}^2e^{2\omega_{1-1}t}). \tag{B3}$$

Note that $\omega_I \ll \omega_R$ in the small-$M\mu$ limit; an important consequence of the latter is the absence of terms proportional to $A_{11}A_{1-1}$ in the above formula. Using Eq. (15), we get

$$M_S(t) = \frac{M_S(0)}{1+\lambda_1^2}(e^{2\omega_{11}t} + \lambda_1^2e^{2\omega_{1-1}t}), \tag{B4}$$

where $M_S(0)$ is the value of M_S at $t=0$. Then, from Eq. (25), we obtain

$$\dot{E}_S = M_S(0)\frac{2}{1+\lambda_1^2}(\omega_{11}e^{2\omega_{11}t} + \omega_{1-1}\lambda_1^2e^{2\omega_{1-1}t}), \tag{B5}$$

which can be expressed as a function of $M_S(t)$, λ_1 and ω_{lm} by isolating $M_S(0)$ in Eq. (B4) and replacing it in the last expression:

$$\dot{E}_S = 2M_S(t)\left(\frac{\omega_{11}e^{2\omega_{11}t} + \lambda_1^2\omega_{1-1}e^{2\omega_{1-1}t}}{e^{2\omega_{11}t} + \lambda_1^2e^{2\omega_{1-1}t}}\right). \tag{B6}$$

Likewise, using Eq. (B1) for the configuration Eq. (B2), we obtain the angular momentum of the condensate,

$$L_S = \frac{32\pi}{M^3\mu^5}(A_{11}^2e^{2\omega_{11}t} - A_{1-1}^2e^{2\omega_{1-1}t}) \tag{B7}$$

or, equivalently,

$$\dot{J}_S = 2\frac{M_S(t)}{\mu}\left(\frac{\omega_{11}e^{2\omega_{11}t} - \lambda_1^2\omega_{1-1}e^{2\omega_{1-1}t}}{e^{2\omega_{11}t} + \lambda_1^2 e^{2\omega_{1-1}t}}\right). \quad \text{(B8)}$$

Note that by using Eqs. (B7) and (B4), the initial angular momentum of the cloud, $L_{S0} \equiv L_S(0)$, is fixed in terms of the initial mass $M_{S0} \equiv M_S(0)$, the initial relative amplitude of the modes λ_{10}, the initial BH parameters M_0 and χ_0, and the gravitational coupling $M_0\mu$.

In the quasiadiabatic approximation, there should not be any explicit time dependence because all the quantities of interest implicitly vary over the time evolution of the system. To remove the explicit time dependence in Eqs. (B6) and (B8), we can consider an average over a time $2\pi/\omega_R \sim 2\pi/\mu$, which is the characteristic orbital time period of the scalar condensate,

$$\langle \dot{E}_S \rangle = 2M_S \int_0^{2\pi/\mu} \mathrm{d}t \frac{\omega_{11}e^{2\omega_{11}t} + \lambda_1^2\omega_{1-1}e^{2\omega_{1-1}t}}{e^{2\omega_{11}t} + \lambda_1^2 e^{2\omega_{1-1}t}}, \quad \text{(B9)}$$

$$\langle \dot{J}_S \rangle = 2\frac{M_S}{\mu} \int_0^{2\pi/\mu} \mathrm{d}t \frac{\omega_{11}e^{2\omega_{11}t} - \lambda_1^2\omega_{1-1}e^{2\omega_{1-1}t}}{e^{2\omega_{11}t} + \lambda_1^2 e^{2\omega_{1-1}t}}, \quad \text{(B10)}$$

where M_S, ω_{11}, and ω_{1-1} are treated as constants. Performing the integrals, we obtain

$$\langle \dot{E}_S \rangle = \frac{M_S\mu}{2\pi}[\ln(e^{\frac{4\pi\omega_{11}}{\mu}} + \lambda_1^2 e^{\frac{4\pi\omega_{1-1}}{\mu}}) - \ln(1+\lambda_1^2)],$$
$$\langle \dot{J}_S \rangle = \frac{(\omega_{11}+\omega_{1-1})\langle \dot{E}_S \rangle}{\mu(\omega_{11}-\omega_{1-1})} - \frac{4M_S\omega_{11}\omega_{1-1}}{\mu(\omega_{11}-\omega_{1-1})}.$$

Finally, by expanding the above relations in the $M\mu \ll 1$ limit, we obtain Eqs. (29)–(30).

3. Model III: $l = 1, 2$ with $m = 1$

At last, let us consider the case of a scalar cloud described by Eq. (13). In this case, the scalar condensate reads

$$\Psi = A_{11}e^{\omega_{11}t}g_1(r)\cos(\phi - \omega_R t)\sin\theta + A_{21}e^{\omega_{21}t}g_2(r)\cos(\phi - \omega_R t)\cos\theta\sin\theta, \quad \text{(B15)}$$

and we obtain

$$\langle \dot{J}_S \rangle = M_S \frac{\{4\pi\omega_{11}\omega_{22} + (\omega_{11} - 2\omega_{22})\mu[\ln(e^{\frac{4\pi\omega_{11}}{\mu}} + 81\lambda_2^2 e^{\frac{4\pi\omega_{22}}{\mu}}) - \ln(1+81\lambda_2^2)]\}}{2\pi\mu(\omega_{11}-\omega_{22})}. \quad \text{(B14)}$$

Finally, by expanding the above relations in the $M\mu \ll 1$ limit, we obtain Eqs. (27)–(28). Note that the final result would be the same if the averages were performed over several orbital periods.

2. Model II: $l = m = 2$ and $l = m = 1$

We now consider the case of a scalar cloud described by Eq. (12). After including the time dependence, the expression of the scalar condensate reads

$$\Psi = A_{11}e^{\omega_{11}t}g_1(r)\cos(\phi - \omega_R t)\sin\theta + A_{22}e^{\omega_{22}t}g_2(r)\cos(2\phi - \omega_R t)\sin^2\theta. \quad \text{(B11)}$$

Using Eq. (B1) for this configuration, we get

$$L_S = \frac{32\pi}{M^3\mu^5}(A_{11}^2 e^{2\omega_{11}t} + 162A_{22}^2 e^{2\omega_{1-1}t}), \quad \text{(B12)}$$

and the same computation described above for model I yields

$$\dot{E}_S = 2M_S(t)\left(\frac{\omega_{11}e^{2\omega_{11}t} + 81\lambda_2^2\omega_{22}e^{2\omega_{22}t}}{e^{2\omega_{11}t} + 81\lambda_2^2 e^{2\omega_{22}t}}\right),$$
$$\dot{J}_S = 2\frac{M_S(t)}{\mu}\left(\frac{\omega_{11}e^{2\omega_{11}t} + 162\lambda_2^2\omega_{22}e^{2\omega_{22}t}}{e^{2\omega_{11}t} + 81\lambda_2^2 e^{2\omega_{22}t}}\right).$$

In this case, the time average gives

$$\langle \dot{E}_S \rangle = \frac{M_S\mu}{2\pi}[\ln(e^{\frac{4\pi\omega_{11}}{\mu}} + 81\lambda_2^2 e^{\frac{4\pi\omega_{22}}{\mu}}) - \ln(1+81\lambda_2^2)], \quad \text{(B13)}$$

$$\dot{E}_S = 2M_S(t)\left(\frac{4\omega_{11}e^{2\omega_{11}t} + 81\lambda_2^3\omega_{21}e^{2\omega_{21}t}}{4e^{2\omega_{11}t} + 81\lambda_3^2 e^{2\omega_{21}t}}\right), \quad \text{(B16)}$$

$$\dot{J}_S = \frac{1}{\mu}\dot{E}_S. \quad \text{(B17)}$$

The last relation is expected because both modes have $m = 1$. In this case, it is sufficient to average Eq. (B16),

$$\langle \dot{E}_S \rangle = \frac{M_S\mu}{2\pi}[\ln(4e^{\frac{4\pi\omega_{11}}{\mu}} + 81\lambda_3^2 e^{\frac{4\pi\omega_{21}}{\mu}}) - \ln(4+81\lambda_3^2)]$$
$$\langle \dot{J}_S \rangle = \frac{1}{\mu}\langle \dot{E}_S \rangle.$$

Again, by expanding the above relations in the $M\mu \ll 1$ limit, we finally obtain Eqs. (31)–(32).

[1] R. Brito, V. Cardoso, and P. Pani, Superradiance, Lect. Notes Phys. **906**, 1 (2015).

[2] Y. B. Zel'dovich, Generation of waves by a rotating body, JETP Lett. **14**, 180 (1971).

[3] T. Damour, N. Deruelle, and R. Ruffini, On quantum resonances in stationary geometries, Lett. Nuovo Cimento **15**, 257 (1976).

[4] S. Teukolsky and W. Press, Perturbations of a rotating black hole. III—Interaction of the hole with gravitational and electromagnet ic radiation, Astrophys. J. **193**, 443 (1974).

[5] W. H. Press and S. A. Teukolsky, Floating orbits, superradiant scattering and the black-hole bomb, Nature (London) **238**, 211 (1972).

[6] Y. Shlapentokh-Rothman, Exponentially growing finite energy solutions for the Klein-Gordon equation on sub-extremal Kerr spacetimes, Commun. Math. Phys. **329**, 859 (2014).

[7] G. Moschidis, Superradiant instabilities for short-range non-negative potentials on Kerr spacetimes and applications, arXiv:1608.02041.

[8] A. Arvanitaki, S. Dimopoulos, S. Dubovsky, N. Kaloper, and J. March-Russell, String Axiverse, Phys. Rev. D **81**, 123530 (2010).

[9] A. Arvanitaki and S. Dubovsky, Exploring the string axiverse with precision black hole physics, Phys. Rev. D **83**, 044026 (2011).

[10] T. Helfer, D. J. E. Marsh, K. Clough, M. Fairbairn, E. A. Lim, and R. Becerril, Black hole formation from axion stars, J. Cosmol. Astropart. Phys. 03 (2017) 055.

[11] T. Helfer, E. A. Lim, M. A. G. Garcia, and M. A. Amin, Gravitational wave emission from collisions of compact scalar solitons, Phys. Rev. D **99**, 044046 (2019).

[12] J. Jaeckel and A. Ringwald, The low-energy Frontier of particle physics, Annu. Rev. Nucl. Part. Sci. **60**, 405 (2010).

[13] R. Essig *et al.*, Working group report: New light weakly coupled particles, in *Proceedings, 2013 Community Summer Study on the Future of U.S. Particle Physics: Snowmass on the Mississippi (CSS2013): Minneapolis, MN, USA, 2013* (2013), http://www.slac.stanford.edu/econf/C1307292/docs/IntensityFrontier/NewLight-17.pdf.

[14] L. Hui, J. P. Ostriker, S. Tremaine, and E. Witten, Ultralight scalars as cosmological dark matter, Phys. Rev. D **95**, 043541 (2017).

[15] I. G. Irastorza and J. Redondo, New experimental approaches in the search for axion-like particles, Prog. Part. Nucl. Phys. **102**, 89 (2018).

[16] S. L. Detweiler, Black holes and gravitational waves. III. The resonant frequencies of rotating holes, Astrophys. J. **239**, 292 (1980).

[17] V. Cardoso, O. J. Dias, and S. Yoshida, Classical instability of Kerr-AdS black holes and the issue of final state, Phys. Rev. D **74**, 044008 (2006).

[18] S. R. Dolan, Instability of the massive Klein-Gordon field on the Kerr spacetime, Phys. Rev. D **76**, 084001 (2007).

[19] S. R. Dolan, Superradiant instabilities of rotating black holes in the time domain, Phys. Rev. D **87**, 124026 (2013).

[20] O. A. Hannuksela, R. Brito, E. Berti, and T. G. F. Li, Probing the existence of ultralight bosons with a single gravitational-wave measurement, Nat. Astron., https://doi.org/10.1038/s41550-019-0712-4 (2019).

[21] M. Isi, L. Sun, R. Brito, and A. Melatos, Directed searches for gravitational waves from ultralight bosons, arXiv:1810.03812.

[22] S. D'Antonio *et al.*, Semicoherent analysis method to search for continuous gravitational waves emitted by ultralight boson clouds around spinning black holes, Phys. Rev. D **98**, 103017 (2018).

[23] D. Baumann, H. S. Chia, and R. A. Porto, Probing ultralight bosons with binary black holes, Phys. Rev. D **99**, 044001 (2019).

[24] M. Boskovic, R. Brito, V. Cardoso, T. Ikeda, and H. Witek, Axionic instabilities and new black hole solutions, Phys. Rev. D **99**, 035006 (2019).

[25] T. Ikeda, R. Brito, and V. Cardoso, Electromagnetic Emission from Axionic Clouds and the Quenching of Superradiant Instabilities, Phys. Rev. Lett. **122**, 081101 (2019).

[26] P. Pani, V. Cardoso, L. Gualtieri, E. Berti, and A. Ishibashi, Black Hole Bombs and Photon Mass Bounds, Phys. Rev. Lett. **109**, 131102 (2012).

[27] P. Pani, V. Cardoso, L. Gualtieri, E. Berti, and A. Ishibashi, Perturbations of slowly rotating black holes: Massive vector fields in the Kerr metric, Phys. Rev. D **86**, 104017 (2012).

[28] R. Brito, V. Cardoso, and P. Pani, Partially massless gravitons do not destroy general relativity black holes, Phys. Rev. D **87**, 124024 (2013).

[29] P. Pani and A. Loeb, Constraining primordial black-hole bombs through spectral distortions of the cosmic microwave background, Phys. Rev. D **88**, 041301 (2013).

[30] S. Endlich and R. Penco, A modern approach to superradiance, J. High Energy Phys. 05 (2017) 052.

[31] V. Cardoso, P. Pani, and T.-T. Yu, Superradiance in rotating stars and pulsar-timing constraints on dark photons, Phys. Rev. D **95**, 124056 (2017).

[32] M. Baryakhtar, R. Lasenby, and M. Teo, Black hole superradiance signatures of ultralight vectors, Phys. Rev. D **96**, 035019 (2017).

[33] H. Witek, V. Cardoso, A. Ishibashi, and U. Sperhake, Superradiant instabilities in astrophysical systems, Phys. Rev. D **87**, 043513 (2013).

[34] V. Cardoso, O. J. C. Dias, G. S. Hartnett, M. Middleton, P. Pani, and J. E. Santos, Constraining the mass of dark photons and axion-like particles through black-hole superradiance, J. Cosmol. Astropart. Phys. 03 (2018) 043.

[35] V. P. Frolov, P. Krtou, D. Kubizk, and J. E. Santos, Massive Vector Fields in Rotating Black-Hole Spacetimes: Separability and Quasinormal Modes, Phys. Rev. Lett. **120**, 231103 (2018).

[36] S. R. Dolan, Instability of the Proca field on Kerr spacetime, Phys. Rev. D **98**, 104006 (2018).

[37] P. Bosch, S. R. Green, and L. Lehner, Nonlinear Evolution and Final Fate of Charged Anti-de Sitter Black Hole Superradiant Instability, Phys. Rev. Lett. **116**, 141102 (2016).

[38] P. M. Chesler and D. A. Lowe, Nonlinear evolution of the AdS_4 black hole bomb, arXiv:1801.09711.

[39] N. Sanchis-Gual, J. C. Degollado, P. J. Montero, J. A. Font, and C. Herdeiro, Explosion and Final State of an Unstable Reissner-Nordstrm Black Hole, Phys. Rev. Lett. **116**, 141101 (2016).

[40] W. E. East and F. Pretorius, Superradiant Instability and Backreaction of Massive Vector Fields around Kerr Black Holes, Phys. Rev. Lett. **119**, 041101 (2017).
[41] W. E. East, Superradiant instability of massive vector fields around spinning black holes in the relativistic regime, Phys. Rev. D **96**, 024004 (2017).
[42] W. E. East, Massive Boson Superradiant Instability of Black Holes: Nonlinear Growth, Saturation, and Gravitational Radiation, Phys. Rev. Lett. **121**, 131104 (2018).
[43] R. Brito, V. Cardoso, and P. Pani, Black holes as particle detectors: Evolution of superradiant instabilities, Classical Quantum Gravity **32**, 134001 (2015).
[44] C. A. R. Herdeiro and E. Radu, Dynamical Formation of Kerr Black Holes with Synchronized Hair: An Analytic Model, Phys. Rev. Lett. **119**, 261101 (2017).
[45] C. A. R. Herdeiro and E. Radu, Kerr Black Holes with Scalar Hair, Phys. Rev. Lett. **112**, 221101 (2014).
[46] C. Herdeiro, E. Radu, and H. Runarsson, Kerr black holes with Proca hair, Classical Quantum Gravity **33**, 154001 (2016).
[47] B. Ganchev and J. E. Santos, Scalar Hairy Black Holes in Four Dimensions are Unstable, Phys. Rev. Lett. **120**, 171101 (2018).
[48] J. C. Degollado, C. A. R. Herdeiro, and E. Radu, Effective stability against superradiance of Kerr black holes with synchronised hair, Phys. Lett. B **781**, 651 (2018).
[49] P. T. Chrusciel, J. L. Costa, and M. Heusler, Stationary black holes: Uniqueness and beyond, Living Rev. Relativity **15**, 7 (2012).
[50] C. A. R. Herdeiro and E. Radu, Asymptotically flat black holes with scalar hair: A review, Int. J. Mod. Phys. D **24**, 1542014 (2015).
[51] A. Arvanitaki, M. Baryakhtar, and X. Huang, Discovering the QCD axion with black holes and gravitational waves, Phys. Rev. D **91**, 084011 (2015).
[52] R. Brito, S. Ghosh, E. Barausse, E. Berti, V. Cardoso, I. Dvorkin, A. Klein, and P. Pani, Gravitational wave searches for ultralight bosons with LIGO and LISA, Phys. Rev. D **96**, 064050 (2017).
[53] S. Ghosh, E. Berti, R. Brito, and M. Richartz, Follow-up signals from superradiant instabilities of black hole merger remnants, arXiv:1812.01620.
[54] R. Brito, S. Ghosh, E. Barausse, E. Berti, V. Cardoso, I. Dvorkin, A. Klein, and P. Pani, Stochastic and Resolvable Gravitational Waves from Ultralight Bosons, Phys. Rev. Lett. **119**, 131101 (2017).
[55] H. Okawa, H. Witek, and V. Cardoso, Black holes and fundamental fields in Numerical Relativity: Initial data construction and evolution of bound states, Phys. Rev. D **89**, 104032 (2014).
[56] M. Zilhão, H. Witek, and V. Cardoso, Nonlinear interactions between black holes and Proca fields, Classical Quantum Gravity **32**, 234003 (2015).
[57] H. Witek and M. Zilhão, Proca fields around rotating black holes (to be published).
[58] E. Berti, V. Cardoso, and M. Casals, Eigenvalues and eigenfunctions of spin-weighted spheroidal harmonics in four and higher dimensions, Phys. Rev. D **73**, 024013 (2006).
[59] V. Cardoso and S. Yoshida, Superradiant instabilities of rotating black branes and strings, J. High Energy Phys. 07 (2005) 009.
[60] P. Pani, Advanced methods in black-hole perturbation theory, Int. J. Mod. Phys. A **28**, 1340018 (2013).
[61] E. Berti, V. Cardoso, and A. O. Starinets, Quasinormal modes of black holes and black branes, Classical Quantum Gravity **26**, 163001 (2009).
[62] S. L. Detweiler, Klein-Gordon equation and rotating black holes, Phys. Rev. D **22**, 2323 (1980).
[63] H. Yoshino and H. Kodama, Bosenova and Axiverse, Classical Quantum Gravity **32**, 214001 (2015).
[64] E. Poisson and M. Sasaki, Gravitational radiation from a particle in circular orbit around a black hole. 5: Black hole absorption and tail corrections, Phys. Rev. D **51**, 5753 (1995).
[65] H. Yoshino and H. Kodama, Bosenova collapse of axion cloud around a rotating black hole, Prog. Theor. Phys. **128**, 153 (2012).
[66] V. Cardoso, P. Pani, M. Cadoni, and M. Cavaglia, Ergoregion instability of ultracompact astrophysical objects, Phys. Rev. D **77**, 124044 (2008).
[67] V. Cardoso, P. Pani, M. Cadoni, and M. Cavaglia, Instability of hyper-compact Kerr-like objects, Classical Quantum Gravity **25**, 195010 (2008).
[68] P. Pani, E. Barausse, E. Berti, and V. Cardoso, Gravitational instabilities of superspinars, Phys. Rev. D **82**, 044009 (2010).
[69] E. Maggio, P. Pani, and V. Ferrari, Exotic compact objects and how to quench their ergoregion instability, Phys. Rev. D **96**, 104047 (2017).
[70] E. Maggio, V. Cardoso, S. R. Dolan, and P. Pani, Ergoregion instability of exotic compact objects: Electromagnetic and gravitational perturbations and the role of absorption, Phys. Rev. D **99**, 064007 (2019).
[71] H. Yoshino and H. Kodama, Gravitational radiation from an axion cloud around a black hole: Superradiant phase, Prog. Theor. Exp. Phys. **2014**, 043E02 (2014).
[72] S. A. Teukolsky, Perturbations of a rotating black hole. 1. Fundamental equations for gravitational electromagnetic and neutrino field perturbations, Astrophys. J. **185**, 635 (1973).
[73] E. Poisson, Gravitational radiation from a particle in circular orbit around a black hole. 1: Analytical results for the nonrotating case, Phys. Rev. D **47**, 1497 (1993).
[74] M. Sasaki and H. Tagoshi, Analytic black hole perturbation approach to gravitational radiation, Living Rev. Relativity **6**, 6 (2003).
[75] S. A. Hughes, Evolution of circular, nonequatorial orbits of Kerr black holes due to gravitational wave emission. 2. Inspiral trajectories and gravitational wave forms, Phys. Rev. D **64**, 064004 (2001).